

**Simulation of Interannual Circulation and Stratification around Placentia Bay**

by

© Yingda Xie

A thesis submitted to the School of Graduate Studies in partial fulfillment of the  
requirements for Master of Science

Department of Physics and Physical Oceanography

Memorial University of Newfoundland

Mar, 2017

St. John's Newfoundland

## Abstract

In this thesis, an application of a three-dimensional, full-prognostic and baroclinic model based on FVCOM is developed to simulate the interannual variability of circulation, sea surface temperature and stratification over Placentia Bay. The model is forced by NARR winds and heat fluxes on the surface and by tides, non-tidal sea level, temperature and salinity on the open boundary. Overall, the model solution compares well with the observed monthly mean water levels, surface currents and SST except for the surface currents at a location near the head of the bay. The circulation patterns in the outer bay area for December 2011 and 2012 showed that the general monthly-mean circulation in the upper ocean were positively correlated with the intensities of the remote westward water inflow from the inshore branch of Labrador Current under geostrophic assumption, which resulted in larger current amplitudes of the cyclonic gyre for December 2012. Over the inner bay, currents in the upper ocean were much weaker due to the reduced effect of the inshore branch of Labrador Current. When the amplitude of the monthly-mean local wind forcing was relatively strong for several months such as October 2010, the wind effect could be as important as the effect of the remote water inflow on the surface circulation. The monthly-mean surface temperature distributions for August 2010 and 2014 showed distinct spatial and interannual variations positively correlated with the observed air temperature, the net heat flux on the sea surface and the water inflow advected from the inshore branch of the Labrador Current. The depth-averaged (0-50m) buoyancy frequency ( $N^2$ ), Richardson Number (Ri) and the mixed layer depth at Buoy-Mouth and Buoy-Red Island also showed interannual variability that

may be positively correlated with the interannual variations of some variables, such as wind intensity, air temperature, and net heat flux.

## Acknowledgment

I would like to say thanks to Prof. **Guoqi Han**, Prof. **Brad de Young** and Dr. **Zhimin Ma** for their assistance and guidance during my graduate program.

Thanks to Dr. Changsheng Chen for providing the FVCOM source code.

## Table of Contents

Abstract	ii
Acknowledgments	iv
List of Tables	vii
List of Figures	viii
Chapter 1 Introduction	1
1.1 Placentia Bay	1
1.2 Oceanographic Observations around Placentia Bay	3
1.3 Model Simulations around Placentia Bay	4
1.4 Objective	6
1.5 Outline	7
Chapter 2 Model Description, Setup and Manipulation	8
2.1 The Governing Equation in Sigma Coordinate	8
2.2 Vertical Integrated Equation (External Mode)	10
2.3 The Turbulent Parameterization Schemes	13
2.4 Model Domain and Grid	18
2.5 Model Surface Forcing	21
2.6 Open Boundary Conditions	24
2.7 Additional Empirical Transport on the Open Boundary	25
2.8 Initial Conditions	28
2.9 Model Runs and Parameterization	29
Chapter 3 Observational Data	31
3.1 Observations of Meteorological Stations	31
3.2 Observations of Mooring Buoys	32
Chapter 4 Model Validation	37
4.1 Data Analysis Method	37
4.2 Validation of Tidal Elevations	39
4.3 Evaluation of Monthly-mean Water Levels	41

4.4 Evaluation of Monthly-mean Surface Currents	44
4.5 Evaluation of Monthly-mean Sea Surface Temperature	53
Chapter 5 Interannual Variability of Monthly-mean Circulation, SST and Stratification	59
5.1 Transports at different Transects	59
5.2 Circulation	64
5.3 Sea Surface Temperature	71
5.4 Stratification and Mixed Layer Depth	74
Chapter 6 Summary and Future Work	80
References	

## List of Tables

Table 4-1: Summary and statistics for observed and computed semi-diurnal and diurnal tidal elevations at coastal tide-gauge stations. Observational locations were shown in Ma (2015).	40
Table 4-2: Statistics from the comparison between observed and simulated monthly-mean sea level anomalies at two tide-gauge stations.	43
Table 4-3: Statistics from the comparison between observed and simulated monthly-mean surface currents (0.5m depth) at Buoy-Mouth.	51
Table 4-4: Statistics from the comparison between observed and simulated monthly-mean surface currents (0.5m depth) at Buoy-Red Island.	52
Table 4-5: Statistics from the comparison between observed and simulated monthly-mean surface currents (0.5m depth) at Buoy-Head.	52
Table 4-6: Statistics from the comparison between observed and simulated monthly-mean SST at Buoy-Mouth.	57
Table 4-7: Statistics from the comparison between observed and simulated monthly-mean SST at Buoy-Red Islands.	58
Table 4-8: Statistics from the comparison between observed and simulated monthly-mean SST at Buoy-Head.	58
Table 4-9: Statistics from the comparison between observed and simulated monthly-mean SST at Buoy- C44251.	58
Table 5-1: Annual statistics of the transports through 53.5°W, 46.9°N and 47.5°N Transect.	62
Table 5-2: Statistics of the simulated SST, observed air temperature and interpolated NARR net heat flux on both Aug 2011 and Aug 2014 at four buoys.	72

## List of Figures

- Fig. 1-1: Map of Placentia Bay and around area showing bathymetry, major locations and observational sites. A is Merasheen Island; B is Red Island and C is Long Island. The red diamonds represent two tide-gauge stations, and the magenta dots are four mooring buoys. 2
- Fig. 2-1: Map of model domain showing the major locations, features and bathymetry (100m and 200m contours). The bathymetry data is from ETOP5. The red and blue lines represent selected transects at east and west open boundary. 19
- Fig. 2-2: The horizontal grid used in this thesis comprised with 25414 nodes and 47629 elements. 20
- Fig. 2-3: Monthly-mean NARR wind speed at 10m high over the sea surface: (a) eastward wind; (b) northward wind. The blue, red and green lines represent NARR wind interpolated onto locations at Buoy-Mouth, Buoy-Red Islands and Buoy-Head. 23
- Fig. 2-4: Monthly-mean NARR net heat flux at sea surface. The blue, red, green and black lines represent NARR net heat flux interpolated onto locations at Buoy-Mouth, Buoy-Red Islands, Buoy-Head and Buoy-c44251. 23
- Fig. 2-5: Monthly-mean transport on selected east open boundary according to HYCOM output (dotted line) and Monthly-mean transport on selected east open boundary according to FVCOM output (solid line). Positive sign means westward direction. 27
- Fig. 2-6: Map showing the Probability Density Function (black line) of the added asymmetric parabolic sea level slope on the selected east open boundary (red line), with the most slope in Avalon Channel. The dotted lines are 100m contour line. 28
- Fig. 3-1: Monthly-mean observed (a) surface eastward current velocity  $U$ , (b) surface northward current velocity  $V$ , and (c) surface wind velocity at three buoys from Sep 2010 to Aug 2014. The blue, red and green lines represent data at Buoy-Mouth, Buoy-Red Island and Buoy-Head. 35
- Fig. 3-2: Monthly-mean SST at four buoys from Sep 2010 to Aug 2014. The blue, red, green and black lines represent data at Buoy-Mouth, Buoy-Red Islands, Buoy-Head and Buoy-c44251. 36

- Fig. 3-3: Monthly-mean Air Temperature at three buoys from Sep 2010 to Aug 2014. The blue, red and green lines represent data at Buoy-Mouth, Buoy-Red Islands and Buoy-Head. 36
- Fig. 4-1: Monthly-mean observed (red) and simulated (blue) sea level anomalies at (a) Argentia and (b) St. Lawrence during Sep 2010 and Aug 2014. 42
- Fig. 4-2: Monthly-mean observed (red) and simulated (blue): surface eastward current velocity (U), surface northward current velocity (V) and surface wind velocity at (a)/(b)/(c) Buoy-Mouth; (c)/(d)/(e) Buoy-Red Islands; and (e)/(f)/(g) Buoy-Head. 47
- Fig. 4-3: Monthly-mean observed (red lines) and simulated (blue lines) SST at: (a) Buoy-Mouth, (b) Buoy-Red Islands, (c) Buoy-Head and (d) Buoy-c44251. 54
- Fig. 5-1: Map showing the three transects used to calculate water transport there. The isobaths displayed are 100 and 200m contour lines. 60
- Fig. 5-2: Seasonal-mean transport on 53.5W Transect (black line) and 46.9N Transect (red line). Positive transport is westward or northward. 62
- Fig. 5-3: Monthly-mean simulated transport (Sv) at four different transects. Positive transport is eastward or northward. 63
- Fig. 5-4: Monthly-mean simulated surface/depth-averaged (0-30m) circulation, horizontal sea level distributions and the corresponding close-ups for the inner bay area of Dec 2011. The spatially-averaged monthly-mean NARR wind vector at 10m high above the ocean is shown in the surface circulation map. 67
- Fig. 5-5: Monthly-mean simulated surface/depth-averaged (0-30m) circulation, horizontal sea level distributions and the corresponding close-ups for the inner bay area of Dec 2012. The spatially-averaged monthly-mean NARR wind vector at 10m high above the ocean is shown in the surface circulation map. 68
- Fig. 5-6: Monthly-mean simulated surface/depth-averaged (0-30m) circulation, horizontal sea level distributions and the corresponding close-ups for the inner bay area of Oct 2010. The spatially-averaged monthly-mean NARR wind vector at 10m high above the ocean is shown in the surface circulation map. 70
- Fig. 5-7: Monthly-mean simulated SST of Aug 2011 and Aug 2014. The spatially-averaged monthly-mean NARR wind vectors at 10m high above the ocean are shown. The blue dots from outer bay to inner bay represent location of Bouy-Mouth, Buoy-Red Island, Buoy-Head and Buoy-c44251. 73

Fig. 5-8: Monthly-mean depth-averaged (0-50m) buoyancy frequency ( $N^2$ ) at: (a) Buoy-Mouth and (b) Buoy-Red Island. 76

Fig. 5-9: Monthly-mean depth-averaged (0-50m) Richardson Number (Ri) at: (a) Buoy-Mouth, (b) Buoy-Red Island. The red lines are critical Richardson Number. 77

Fig. 5-10: Monthly-mean Mixed Layer Depth at: (a) Buoy-Mouth and (b) Buoy-Red Island. 79

## List of Symbols and Abbreviation

$\sigma$	Sigma coordinate from 0 to -1
$\zeta$	Free surface elevation (m)
<b>D</b>	Water depth plus sea level (m)
<b>H</b>	Bottom depth (m)
$K_m$	Vertical turbulent viscosity ( $m^2/s$ )
$K_h$	Vertical diffusivity ( $m^2/s$ )
$\rho$	Potential density ( $kg/m^3$ )
$A_m$	Horizontal viscosity ( $m^2/s$ )
$A_h$	Horizontal diffusivity ( $m^2/s$ )
<b>T</b>	Potential temperature ( $^{\circ}C$ )
<b>S</b>	Salinity ( <i>psu</i> )
$q^2$	Twice the turbulent kinetic energy ( $m^2/s^2$ )
<b>l</b>	Turbulent length scale
<b>u</b>	Eastward velocity (m/s)
<b>v</b>	Northward velocity (m/s)
$\omega$	Sigma coordinate vertical velocity (m/s)
$\kappa$	Von Karman constant = 0.4
<b>Sv</b>	Sverdrup
<b>Jan</b>	January
<b>Feb</b>	February
<b>Mar</b>	March
<b>Apr</b>	April
<b>Jun</b>	June
<b>Jul</b>	July

<b>Aug</b>	August
<b>Sep</b>	September
<b>Oct</b>	October
<b>Nov</b>	November
<b>Dec</b>	December
<b>Var</b>	Variance
<b>NaN</b>	Not a Number
<b>SST</b>	Sea Surface Temperature
<b>SDR</b>	Speed Difference Ratio
<b>VDR</b>	Velocity Difference Ratio
<b>MLD</b>	Mixed Layer Depth
<b>RMSD</b>	Root-Mean-Square Difference
<b>GOTM</b>	Global Ocean Turbulent Model
<b>HYCOM</b>	HYbrid Coordinate Ocean Model
<b>FVCOM</b>	Finite Volume Coastal Ocean Model
<b>Spring</b>	From April to June
<b>Summer</b>	From July to September
<b>Fall</b>	From October to December
<b>Winter</b>	From January to March

## **1. Introduction**

### **1.1 Placentia Bay**

Placentia Bay (Fig 1-1) is located on the southeast coast of Newfoundland, Canada. It is oriented approximately northeast to southwest. It is bounded by the Burin Peninsula on the west and the Avalon Peninsula on the east, with its head located southwest of Arnold's Cove and its mouth extending into the North Atlantic Ocean. There are three large islands located in the north-central part of the bay, Merasheen Island, Red Island and Long Island (Points A, B and C in Fig 1-1). The bay is about 130 km long and about 100 km wide at the mouth of the bay. The eastern side of the bay has a relatively regular and straight coastline, while the head and western side of the bay have many islands and an irregular coastline. The center of the outer bay is about 200 m deep, while much of the remainder of the outer bay is typically 100 m deep. The average depth of the Bay is around 125 m although there are several 400 m deep channels that run along the longitudinal axis of the inner bay. Winds are predominantly from the southwest and west from spring until fall and from the northwest and west in winter. There are frequent extratropical storms in winter and spring and occasional tropical storms in summer and fall (Catto et al., 1997). There are important fisheries on the western side of the bay (Rose et al., 1999; Bradbury et al., 2000; Lawson and Rose 2000; Snelgrove et al., 2008; Bradbury et al., 2008;) and heavy ship traffic on the eastern side of the bay (near Argentia). These two activities have stimulated many progressive investigations about oceanic dynamics in this coastal area through observations and model simulations.

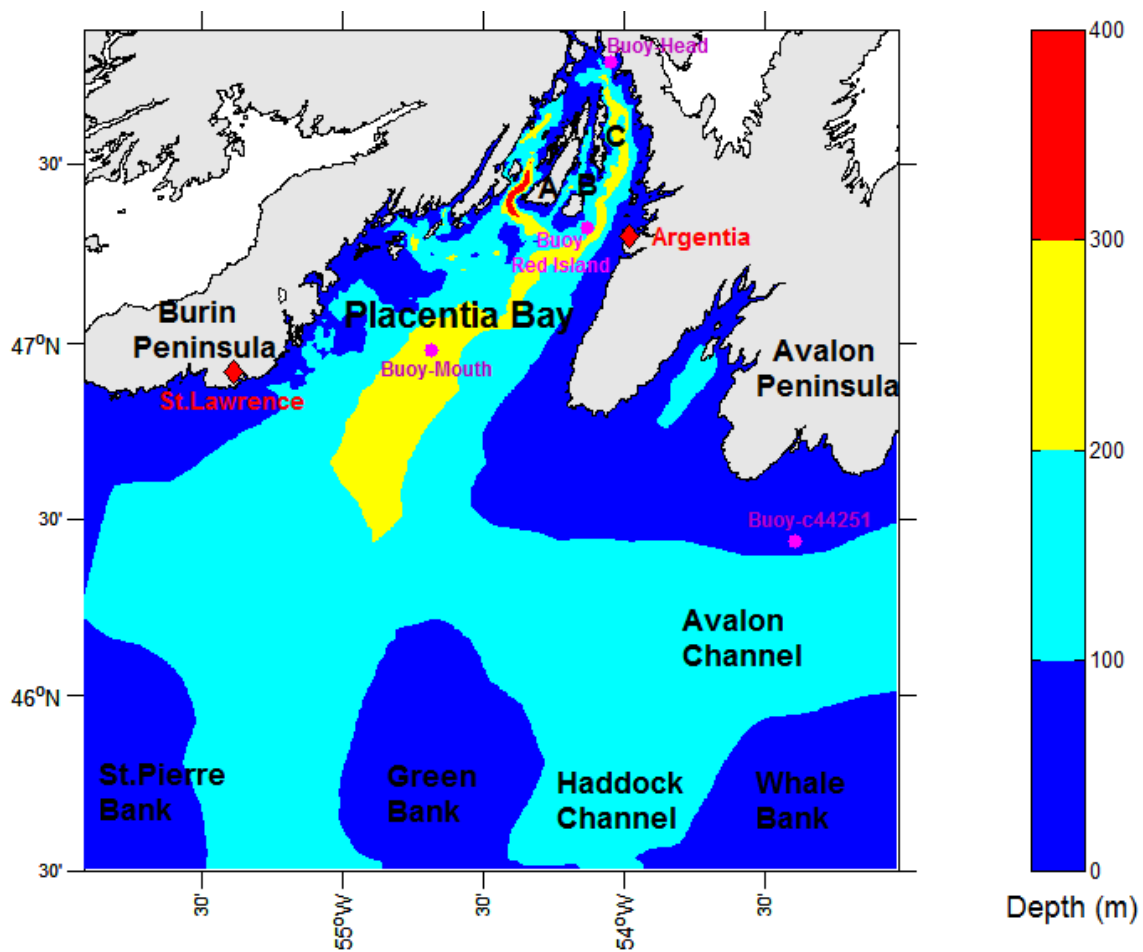


Fig 1-1: Map of Placentia Bay and around area showing bathymetry, major locations and observational sites. A is Merasheen Island; B is Red Island and C is Long Island. The red diamonds represent two tide-gauge stations, and the magenta dots are four mooring buoys.

## 1.2 Oceanographic Observations around Placentia Bay

In last few decades data from various *in situ* observations in the Placentia Bay region have been collected and analysed. Based on various historical observations from drifters, current meters, buoys and tide gauge stations, Petrie and Anderson (1983) estimated the mean circulation and transport on the Newfoundland Continental Shelf, indicating a mean flow of the inshore branch of Labrador Current through the Avalon Channel into Placentia Bay. Hart et al. (1999) and Scillinger et al. (2000) deployed four moorings in April-July, 1998 and seven in 1999 in Placentia Bay to observe the mean seasonal circulation pattern together with seasonal current variability and hydrographic changes. According to their analysis, the mean circulation in the outer bay during spring and summer is mainly driven by the westward current of the inshore branch of Labrador Current that flows into the bay on the eastern side, continues along the coastline and flows out of the bay on the western side. Meanwhile, much local variation also exists, especially over the inner bay area, which may be due to local wind forcing (deYoung et al. 1993). However, neither the spatial coverage nor the temporal duration of the analysed observations around Placentia Bay is enough to investigate its low-frequency circulation, transport, hydrography and mixing for all seasons or multi-years.

Since 2006, three Meteorological/Oceanographic buoys were deployed as part of the SmartAtlantic Alliance (Hogan, 2008) at head, center and mouth of Placentia Bay, observing currents, waves, sea surface temperature, sea surface salinity and weather conditions of the bay. There are also two Environmental-Canada meteorological stations observing sea level and weather conditions, one at Argentia, located on the eastern side of

the middle bay, the other at St. Lawrence located on the western side of the outer bay. Both these data sources offer opportunity for oceanographers to study coastal dynamics around Placentia Bay through direct data analysis and model validation.

### **1.3 Model Simulations around Placentia Bay**

There have been many numerical studies on regional- and coastal- ocean dynamics over the Newfoundland Shelf and its embayments including Placentia Bay, providing coastal dynamical understandings of Placentia Bay at different spatial and temporal scales.

On tidal scales, Han (2000) set up a three-dimensional barotropic tide model with five major tidal constituents to detect substantial variability of tidal currents and associated mixing over the Grand Bank and its vicinity, showing that the dominant M2 tide propagated southwestward along the Newfoundland coast as a coastal Kelvin wave, with the amplitude reaching 70 *cm* in Placentia Bay. Ma et al. (2012) simulated tidal elevations and tidal currents around Placentia Bay based on a finite-volume coastal ocean model (FVCOM), which was forced on the open boundary by five major tidal constants interpolated from a shelf model over the Grand Banks of Newfoundland (Han et al., 2011). The co-amplitude/phase charts and current ellipses of all five tides agree well with tide gauges and previous model results (Han, 2000; Han et al., 2010).

At the weather-band time scale, Ma et al. (2012) simulated non-tidal sea level, non-tidal currents and temperature around Placentia Bay during April and June, 1999 and found reasonable agreement with moored measurements from Hart et al. (1999). The simulated non-tidal sea level was found to be correlated with wind strength and direction.

The simulated surface currents and SST fields at two specific moments showed two distinct circulation patterns: a cyclonic circulation steering into the bay and flowing out along the western side of the bay in late April due to remote effect from inshore branch of the Labrador Current; coastal upwelling on the west coast and offshore transport of low temperature water near 47°N in late June due to local wind effect. Ma (2015) developed a three-dimensional, baroclinic, finite-volume coast ocean model (FVCOM) to simulate the response of Placentia Bay to Hurricane Igor (2010) and Hurricane Leslie (2012). Before and after the hurricanes, the model reproduced the general cyclonic circulation in the inner bay. During the two hurricanes, which had different tracks and strength, the model indicated different contributions to storm surges from local wind forcing or remote coastally trapped waves, and different upper-layer circulations, either overcome or strengthen the general cyclonic circulation. The importance of stratification in simulation of wind induced events was also examined.

At longer time scales, several different regional models have been used to investigate the seasonal and interannual variability of circulation and transport over the Newfoundland Shelf and its embayments, including Placentia Bay. Greenberg and Petrie (1988) presented the mean barotropic circulation over the Grand Banks, showing notable discrepancies between observed and simulated westward flow around outer Placentia Bay from the inshore branch of Labrador Current. A diagnostic calculation of summer surface circulation by Shen et al. (1996) also showed westward currents from the inshore branch of Labrador Current flowing into the outer Placentia Bay on eastern side and out on western side. Han (2005) investigated the barotropic wind-driven circulation over the Newfoundland and Labrador shelf during the whole 1990s based on a diagnostic finite

element model, indicating prominent seasonal and interannual variability for the inshore branch of Labrador Current, which was significantly contributed to local wind forcing. Han et al. (2008) presented climatological monthly-mean wind- and density-driven circulation off Newfoundland based on a semi-prognostic finite element model, with a strategy of sufficient refinement through the restoring approach to reach a quasi-steady dynamic equilibrium among the prognostic variables. Han et al. (2011) improved the climatological monthly-mean wind- and density-driven circulation off Newfoundland by using a prognostic finite-volume coastal ocean model (FVCOM), and at the same time, presented a hindcast for spring to fall of 1999 which showed reasonable skill in reproducing temperature, salinity and currents. Urrego-Blanco and Sheng (2012) simulated the seasonal and interannual variability over the eastern Canadian continental shelf by applying the spectral nudging method. However, these shelf models all had insufficient resolution for Placentia Bay, and thus offer little insight into circulation of the Bay. Although Ma et al. (2012) analyzed the circulation and mixing around Placentia Bay during April and November of 1999, its low-frequency variabilities and the mechanisms behind them among all seasons (especially winter season) or several years are still not clear. Thus, a long-term, full-prognostic coastal model with a focus on Placentia Bay is needed to complement the observations of the Smart Bay Project.

#### **1.4 Objective**

Considering several previous successful short-term applications of Finite Volume Coastal Ocean Model (FVCOM) in Newfoundland Shelf and Placentia Bay, and some long-term applications of FVCOM experiences in other coastal areas (Cowles et al., 2008;

Long Jiang et al., 2016), the objective of this thesis is to develop a long-term (four consecutive years), three-dimensional, full-prognostic and baroclinic model based on FVCOM for Placentia Bay. The model should be able to accurately simulate sea level, currents and temperature there (the model solution will be compared against independent observational mooring and tide-gauge data); analyze monthly-mean circulation, sea surface temperature and stratification during the simulation period, determine the roles of various factors played on the interannual variabilities, and explain physical mechanisms behind them.

## **1.5 Outline**

Chapter 2 describes the basic equations of FVCOM, grid generation, surface forcing, initial/open boundary conditions and model running. The observational moorings and tide-gauge data used for model validation are analyzed in chapter 3. Section 4 presents validation and evaluation of simulated monthly-mean sea level, surface currents and SST compared to independent observations. Chapter 5 discusses interannual variability of circulation, sea surface temperature and stratification; chapter 6 is the summary.

## 2. Model Description, Setup and Manipulation

### 2.1 The Governing Equation in Sigma Coordinate

The numerical model used for this study is an unstructured grid, primitive equation, three-dimensional finite-volume coastal ocean model (FVCOM; Chen et al., 2003), which has been successfully applied over Newfoundland Shelf and its embayments by Han et al. (2011), Ma et al. (2012) and Ma (2015). Unlike the differential form used in finite-difference and finite-element models, FVCOM discretizes the integral form of the governing equations. Since these integral equations can be solved numerically by flux calculation (like the finite-difference method) over an arbitrarily sized triangular mesh (like the finite-element method), the finite-volume approach is better suited to guarantee mass conservation in both the individual control element and the entire computational domain. From a technical point of view, FVCOM combines the best attributes of finite-difference methods for simple discrete coding and computational efficiency and finite-element methods for geometric flexibility.

The basic equations could be presented in a terrain following, generalized coordinate system in order to obtain a smooth representation of irregular variable bottom topography. The coordinate transformation is defined as  $\hat{g} = \hat{g}(x, y, r, t)$ , where  $x$  and  $y$  are defined as the eastward and northward axes, and  $r$  varies from -1 at the bottom to 0 at the surface. The term  $r$  can be specified as a sigma ( $\sigma$ ), hybrid or more generalized function.

In this thesis, sigma-coordinates are chosen to better resolve the relative shallow topography around Placentia Bay, where  $r$  is specified as a sigma transformation  $\sigma =$

$\frac{z-\zeta}{H+\zeta} = \frac{z-\zeta}{D}$ , where  $\sigma$  varies from -1 at the bottom to 0 at surface. The total water depth is

$D = H + \zeta$ , where  $H$  is the bottom depth (relative to  $z=0$ ) and  $\zeta$  is the height of the free surface (relative to  $z=0$ ).

In  $\sigma$ -coordinates, the momentum and continuity equations are given as (2.1)-(2.3) under absence of snow and ice, where  $u$ ,  $v$  and  $\omega$  are the eastward, northward and vertical velocity,  $K_m$  and  $\rho_0$  are turbulent viscosity and potential density; the temperature, salinity and density equations are given as (2.4)-(2.6), where  $T$ ,  $S$  and  $\rho$  are temperature, salinity and fluid density,  $K_h$  is vertical diffusivity,  $\hat{H}$  is heat term.

$$\frac{\partial \zeta}{\partial t} + \frac{\partial Du}{\partial x} + \frac{\partial Dv}{\partial y} + \frac{\partial \omega}{\partial \sigma} = 0 \quad (2.1)$$

$$\begin{aligned} & \frac{\partial uD}{\partial t} + \frac{\partial u^2D}{\partial x} + \frac{\partial uvD}{\partial y} + \frac{\partial u\omega}{\partial \sigma} - fvD \\ & = -gD \frac{\partial \zeta}{\partial x} - \frac{gD}{\rho_0} \left[ \frac{\partial}{\partial x} \left( D \int_{\sigma}^0 \rho d\sigma' \right) + \sigma \rho \frac{\partial D}{\partial x} \right] + \frac{1}{D} \frac{\partial}{\partial \sigma} \left( K_m \frac{\partial u}{\partial \sigma} \right) + DF_x \end{aligned} \quad (2.2)$$

$$\begin{aligned} & \frac{\partial vD}{\partial t} + \frac{\partial uvD}{\partial x} + \frac{\partial v^2D}{\partial y} + \frac{\partial v\omega}{\partial \sigma} - fuD \\ & = -gD \frac{\partial \zeta}{\partial y} - \frac{gD}{\rho_0} \left[ \frac{\partial}{\partial y} \left( D \int_{\sigma}^0 \rho d\sigma' \right) + \sigma \rho \frac{\partial D}{\partial y} \right] + \frac{1}{D} \frac{\partial}{\partial \sigma} \left( K_m \frac{\partial v}{\partial \sigma} \right) + DF_y \end{aligned} \quad (2.3)$$

$$\frac{\partial TD}{\partial t} + \frac{\partial TuD}{\partial x} + \frac{\partial TvD}{\partial y} + \frac{\partial T\omega}{\partial \sigma} = \frac{1}{D} \frac{\partial}{\partial \sigma} \left( K_h \frac{\partial T}{\partial \sigma} \right) + D\hat{H} + DF_T \quad (2.4)$$

$$\frac{\partial SD}{\partial t} + \frac{\partial SuD}{\partial x} + \frac{\partial SvD}{\partial y} + \frac{\partial S\omega}{\partial \sigma} = \frac{1}{D} \frac{\partial}{\partial \sigma} \left( K_h \frac{\partial S}{\partial \sigma} \right) + DF_S \quad (2.5)$$

$$\rho = \rho(T, S) \quad (2.6)$$

The horizontal diffusion terms are defined as:

$$DF_x \approx \frac{\partial}{\partial x} [2A_m H \frac{\partial u}{\partial x}] + \frac{\partial}{\partial y} [A_m H (\frac{\partial u}{\partial y} + \frac{\partial v}{\partial x})] \quad (2.7)$$

$$DF_y \approx \frac{\partial}{\partial y} [2A_m H \frac{\partial v}{\partial y}] + \frac{\partial}{\partial x} [A_m H (\frac{\partial u}{\partial y} + \frac{\partial v}{\partial x})] \quad (2.8)$$

$$D(F_T, F_S, F_{q^2}, F_{q^2 l}) \approx [\frac{\partial}{\partial x} (A_h H \frac{\partial}{\partial x}) + \frac{\partial}{\partial y} (A_h H \frac{\partial}{\partial y})](T, S, q^2, q^2 l) \quad (2.9)$$

where  $A_m$  and  $A_h$  are horizontal eddy viscosity and eddy diffusivity, respectively.

## 2.2 Vertical Integrated Equation (External Mode)

FVCOM (version 3.1.4) uses a time splitting method (Madala and Piacsek, 1977) for computational efficiency including the internal mode and external mode. The external mode is for the fast moving motion, while the internal mode is responsible for the slow moving motion. Since a fast moving gravity wave exists in the ocean, sea level should be computed for the external mode. Because sea level is proportional to the gradient of water transport, it can be computed using the vertically integrated equations as (2.10)-(2.12). Then the three-dimensional internal mode equations can be solved for a given sea level. Both modes are constrained by the Courant-Friedrichs-Levy (CFL) condition (Courant et al., 1928). A modified fourth-order Runge-Kutta time-stepping scheme is used for the external time integration with a second-order temporal accuracy, while a first order Euler time stepping scheme is selected for the internal time integration. A second-order accurate upwind scheme, which is based piecewise for linear reconstruction of dynamic variable, is used for the spatial flux calculation for momentum and tracer values (Kobayashi et al., 1999; Hubbard, 1999). For a more accurate estimate of sea level,

currents, and T/S flux,  $u$  and  $v$  are placed at centroids, while all scalar variables are placed at nodes. Similar to finite-difference models, all the model variables except  $\omega$  (vertical velocity at the sigma level) and turbulence variables (such as  $q^2$  and  $q^2l$ ) are placed at the mid-layer of each sigma level. There are no restrictions on the thickness of the sigma level, which allows users to use either uniform or non-uniform sigma levels.

$$\frac{\partial \zeta}{\partial t} + \frac{\partial(\bar{u}D)}{\partial x} + \frac{\partial(\bar{v}D)}{\partial y} = 0 \quad (2.10)$$

$$\begin{aligned} \frac{\partial \bar{u}D}{\partial t} + \frac{\partial \bar{u}^2 D}{\partial x} + \frac{\partial \bar{u}\bar{v}D}{\partial y} - f\bar{v}D = D\bar{F}_x + G_x + \frac{\tau_{sx} - \tau_{bx}}{\rho_0} - gD \frac{\partial \zeta}{\partial x} \\ - \frac{gD}{\rho_0} \left[ \int_{-1}^0 \frac{\partial}{\partial x} \left( D \int_{\sigma}^0 \rho d\sigma' \right) d\sigma + \frac{\partial D}{\partial x} \int_{-1}^0 \sigma \rho d\sigma \right] \end{aligned} \quad (2.11)$$

$$\begin{aligned} \frac{\partial \bar{v}D}{\partial t} + \frac{\partial \bar{v}^2 D}{\partial y} + \frac{\partial \bar{u}\bar{v}D}{\partial x} - f\bar{u}D = D\bar{F}_y + G_y + \frac{\tau_{sy} - \tau_{by}}{\rho_0} - gD \frac{\partial \zeta}{\partial y} \\ - \frac{gD}{\rho_0} \left[ \int_{-1}^0 \frac{\partial}{\partial y} \left( D \int_{\sigma}^0 \rho d\sigma' \right) d\sigma + \frac{\partial D}{\partial y} \int_{-1}^0 \sigma \rho d\sigma \right] \end{aligned} \quad (2.12)$$

The right hand side of the momentum equations (2.11)-(2.12) contains horizontal diffusion, dispersion, wind stress, barotropic and baroclinic term separately.  $G_x$  and  $G_y$  on the left hand side are defined as

$$G_x = \frac{\partial \bar{u}^2 D}{\partial x} + \frac{\partial \bar{u}\bar{v}D}{\partial y} - D\tilde{F}_x - \left[ \frac{\partial \bar{u}^2 D}{\partial x} + \frac{\partial \bar{u}\bar{v}D}{\partial y} - D\bar{F}_x \right] \quad (2.13)$$

$$G_y = \frac{\partial \bar{v}^2 D}{\partial y} + \frac{\partial \bar{u}\bar{v}D}{\partial x} - D\tilde{F}_y - \left[ \frac{\partial \bar{v}^2 D}{\partial y} + \frac{\partial \bar{u}\bar{v}D}{\partial x} - D\bar{F}_y \right] \quad (2.14)$$

and the horizontal diffusion terms are approximately given as

$$D\tilde{F}_x \approx \frac{\partial}{\partial x} [2\bar{A}_m H \frac{\partial \bar{u}}{\partial x}] + \frac{\partial}{\partial y} [\bar{A}_m H (\frac{\partial \bar{u}}{\partial y} + \frac{\partial \bar{v}}{\partial x})] \quad (2.15)$$

$$D\tilde{F}_y \approx \frac{\partial}{\partial y} [2\overline{A_m H} \frac{\partial \bar{v}}{\partial y}] + \frac{\partial}{\partial x} [\overline{A_m H} (\frac{\partial \bar{u}}{\partial y} + \frac{\partial \bar{v}}{\partial x})] \quad (2.16)$$

$$D\bar{F}_x \approx \frac{\partial}{\partial x} \overline{2A_m H \frac{\partial u}{\partial x}} + \frac{\partial}{\partial y} \overline{A_m H (\frac{\partial u}{\partial y} + \frac{\partial v}{\partial x})} \quad (2.17)$$

$$D\bar{F}_y \approx \frac{\partial}{\partial y} \overline{2A_m H \frac{\partial v}{\partial y}} + \frac{\partial}{\partial x} \overline{A_m H (\frac{\partial u}{\partial y} + \frac{\partial v}{\partial x})} \quad (2.18)$$

The overbar “-“denotes the vertical integration.  $\bar{u}$  and  $\bar{v}$  are vertically averaged eastward and northward velocity.  $\tau_{sx}$  and  $\tau_{bx}$  are surface and bottom stress.

The surface boundary conditions at  $r = 0$  are given as follows:

$$\left( \frac{\partial u}{\partial r}, \frac{\partial v}{\partial r} \right) = \frac{J}{\rho_0 K_m} (\tau_{sx}, \tau_{sy}); \quad \omega = 0 \quad (2.19)$$

$$\frac{\partial T}{\partial r} = \frac{J}{\rho c_p K_h} [Q_n(x, y, t) - SW(x, y, 0, t)]; \quad \frac{\partial S}{\partial r} = 0 \quad (2.20)$$

where  $Q_n(x, y, t)$  is the surface net heat flux including net downward shortwave radiation, net downward longwave radiation, sensible fluxes and latent fluxes,  $c_p$  is specific heat of seawater, and  $SW(x, y, 0, t)$  is shortwave flux incident at the sea surface, which means part of the downward shortwave irradiance is penetrated to sub-surface ocean, the amount of which is calculated in the heat term  $\hat{H}$  of the temperature equation (2-4) in the form of:

$$\hat{H}(x, y, z, t) = \frac{\partial SW(x, y, z, t)}{\partial z} = \frac{SW(x, y, 0, t)}{\rho c_p} \left[ \frac{R}{a} e^{\frac{z}{a}} + \frac{1-R}{b} e^{\frac{z}{b}} \right] \quad (2.21)$$

where  $a$  and  $b$  are attenuation lengths for longer and shorter (blue-green) wavelength components of the shortwave irradiance,  $R$  is the percentage of the total flux associated with longer wavelength irradiance. This approach was first suggested by Kraus (1972)

and then applied to numerical studies of upper ocean diurnal heating by Simpson and Dickey (1981a, b).

Because there is no significant river runoff into Placentia Bay, the present model did not include the freshwater input from the river runoff. The kinematic, heat and salt flux conditions on the lateral solid boundary are specified as zero.

### 2.3 The Turbulent Parameterization Schemes

The primitive equations described above are not mathematically closed unless eddy coefficients for momentum, temperature and salinity are determined, which represent the aggregate effects of Reynolds stresses and unresolved sub-grid-scale turbulent motions.

Shear in the mean flow generate instabilities (turbulence), which are manifested by a population of many eddies from a macroscale at which the energy is extracted from the mean flow to a microscale at which energy is dissipated by viscosity (Kolmogorov, 1941). The interactions among these eddies pass energy gradually from the larger ones to the smaller ones, known as the “turbulent energy cascade”. Within the cascade, the Reynolds number is so large that the evolution is fast compared with the decay time due to viscosity. Nonlinear advection is therefore dominant, transferring energy from the largest eddies to the smallest ones without appreciable loss to viscosity. In other words, the dissipation rate  $\varepsilon$  is conserved across the cascade.

Let us denote  $u_v, l_v$  as the velocity scale and length scale of the smallest eddies, and  $u_m, l_m$  as the velocity scale and length scale of the largest eddies. The dissipation rate  $\varepsilon$  is determined by equation (2.21), where  $c_\mu^0$  is a calibration constant.

$$\varepsilon = \left(\frac{c_\mu^0}{4}\right)^{3/4} \frac{u_v^3}{l_v} = \left(\frac{c_\mu^0}{4}\right)^{3/4} \frac{u_m^3}{l_m} \quad (2.21)$$

At the smallest scale of eddies, the cascade stops and the viscous friction becomes a dominant term in the momentum equation, that is, the scale that renders the Reynolds number, ratio of inertia to friction in equation (2.22), of order unity.

$$\frac{u\partial u/\partial x}{\nu\partial^2 u/\partial x^2} \sim \frac{u_v^2/l_v}{\nu u_v/l_v^2} \sim \frac{u_v l_v}{\nu} \sim 1 \quad (2.22)$$

According to Cushman-Roisin and Beckers, (2011), the total turbulent kinetic energy  $k$  at the macroscale does not differ much from that of the largest eddies (equation 2.23), which means the effect of the cascade could be represented via an eddy viscosity  $\nu_E$  at the largest scale, and the dissipation introduced by  $\nu_E$  must extract the  $\varepsilon$  energy per time. To accomplish this, the Reynolds number based on  $\nu_E$  must be on the order of unity at the level of  $l_m$  (equation 2.23). Here, the properties of the turbulent cascade are limited to purely local (so-called one-point closure model).

$$k = \frac{u_m^2}{2}, \quad \frac{u_m l_m}{\nu_E} \sim 1 \quad (2.23)$$

The eddy viscosity concept ensures that fluid parcels moving with the eddy velocity  $u_m$  over the distance  $l_m$  exchange momentum, heat and salt with other fluids parcels, as in molecular diffusion. In summary, in order to calculate the eddy viscosity and complete the closure model, the scales  $u_m$  and  $l_m$ , or  $k$  and  $\varepsilon$  need to be simulated or prescribed.

### 2.3.1 The Horizontal Turbulent Parameterization

Horizontal and vertical directions are treated differently by assigning two distinct

eddy coefficients considering the anisotropy of the flow field and its modeling grid. Because turbulent motions and mesh size cover longer distances in the horizontal than in the vertical, the horizontal eddy coefficients cover a much larger span of unresolved motions and need to be significantly larger than the vertical ones, each of which should be expected to exhibit some spatial variation.

The horizontal eddy coefficients in FVCOM can be selected as a constant value or following the Smagorinsky eddy parameterization method (Smagorinsky, 1963). The horizontal eddy viscosity  $A_m$  and eddy diffusivity  $A_h$  can be expressed by (2.24)-(2.25) using the Smagorinsky method:

$$A_m = 0.5C\Omega^u \sqrt{\left(\frac{\partial u}{\partial x}\right)^2 + 0.5\left(\frac{\partial v}{\partial x} + \frac{\partial u}{\partial y}\right)^2 + \left(\frac{\partial v}{\partial x}\right)^2} \quad (2.24)$$

$$A_h = \frac{0.5C\Omega^\zeta}{P_r} \sqrt{\left(\frac{\partial u}{\partial x}\right)^2 + 0.5\left(\frac{\partial v}{\partial x} + \frac{\partial u}{\partial y}\right)^2 + \left(\frac{\partial v}{\partial x}\right)^2} \quad (2.25)$$

where  $C$  is a constant parameter from 0.1 to 0.2,  $\Omega^u$  and  $\Omega^\zeta$  are the area of the individual momentum control volume and the tracer (such as temperature) control volume.  $P_r$  is the horizontal Prandtl Number, which is the ratio of horizontal eddy diffusivity to horizontal eddy viscosity. In this study,  $P_r$  is set to 1.

Normally, using the same value of horizontal eddy coefficients for energy (tracers) as for momentum is generally adequate, because the larger turbulent motions and subgrid processes act to disperse heat and salt as effectively as momentum.

### 2.3.2 The Vertical Turbulent Parameterization

There has been a wide choice of ocean turbulence closure models for the parameterization of the vertical eddy viscosity  $K_m$  and vertical eddy diffusivity  $K_h$ . The default option in FVCOM (Version 3.1.4) is the updated version of Mellor-Yamada (1982) level 2.5 (MY-2.5) turbulent closure model, which has been the most popular second-order  $q^2$ - $q^2l$  closure model (where  $q^2$  is the turbulent kinetic energy as  $k$ , and  $l$  is the turbulent macroscale as  $l_m$  mentioned above). FVCOM also features the second-order  $k$ - $\varepsilon$  turbulent closure models implemented by the General Ocean Turbulent Model (GOTM) (Burchard, 2001). The  $k$ - $\varepsilon$  model is very similar in structure and dynamics to the  $q^2$ - $q^2l$  turbulent model according to equations (2.21)-(2.23).

For Mellor-Yamada  $q^2$ - $q^2l$  model, the governing equations are given as

$$\frac{\partial q^2}{\partial t} + u \frac{\partial q^2}{\partial x} + v \frac{\partial q^2}{\partial y} + w \frac{\partial q^2}{\partial z} = 2(P_s + P_b - \varepsilon) + \frac{\partial}{\partial z} \left( K_q \frac{\partial q^2}{\partial z} \right) \quad (2.26)$$

$$\frac{\partial q^2 l}{\partial t} + u \frac{\partial q^2 l}{\partial x} + v \frac{\partial q^2 l}{\partial y} + w \frac{\partial q^2 l}{\partial z} = l E_1 \left( P_s + P_b - \frac{\tilde{W}}{E_1} \varepsilon \right) + \frac{\partial}{\partial z} \left( K_q \frac{\partial q^2 l}{\partial z} \right) \quad (2.27)$$

$$K_m = l q S_m, K_h = l q S_h, K_q = 0.2 l q \quad (2.28)$$

where  $K_q$  is the vertical eddy diffusion coefficient of the turbulent kinetic energy;  $P_s = K_m (u_z^2 + v_z^2)$  and  $P_b = (g K_h \rho_z) / \rho_0$  are the shear and buoyancy production terms of turbulent kinetic energy;  $W$  is a wall proximity function;  $S_m$  and  $S_h$  are stability functions depend only on  $G_h = \frac{l^2 g}{q^2 \rho_0} \rho_z$  according to Galperin et al. (1988).

For GOTM  $k$ - $\varepsilon$  model, the governing equations are given as

$$\frac{\partial k}{\partial t} - \frac{\partial}{\partial z} \left( \frac{v_t}{\sigma_k} \frac{\partial k}{\partial z} \right) = P + G - \varepsilon \quad (2.29)$$

$$\frac{\partial \varepsilon}{\partial t} - \frac{\partial}{\partial z} \left( \frac{v_t}{\sigma_\varepsilon} \frac{\partial \varepsilon}{\partial z} \right) = c_1 (P + c_3 G) \frac{\varepsilon}{k} - c_2 \frac{\varepsilon^2}{k} \quad (2.30)$$

$$v_t = c_\mu \frac{k^2}{\varepsilon} \quad (2.31)$$

where  $v_t$  is vertical the eddy viscosity (same as  $K_q$  in the  $q^2$ - $q^2l$  model),  $\sigma_k$  and  $\sigma_\varepsilon$  is the vertical Prandtl number that is defined as the ratio of vertical eddy viscosity to vertical thermal diffusivity, which are depend on the Richardson Number  $R_i$ ;  $P$  and  $G$  are turbulent shear and buoyancy production (same as  $P_s$  and  $P_b$  in the  $q^2$ - $q^2l$  model);  $c_\mu$  is either a constant or a function of vertical shear of the horizontal velocity and vertical stratification;  $c_1$ ,  $c_2$  and  $c_3$  are empirical constants.

The biggest difference between these two closure models is the cutoff of mixing by setting a critical Richardson Number  $R_i$ . In the  $q^2$ - $q^2l$  model, the critical  $R_i$  is set as 0.25 based upon linear stability analysis according to Miles (1961). This critical number means the turbulence cannot exist for  $R_i > 0.25$ . However, while this relation is necessary, it's not a sufficient condition for stability, since it says nothing about nonlinearities and the related turbulence (Abarbanel et al., 1984). Therefore, in the  $k$ - $\varepsilon$  model, Canuto et al. (2001) set the critical  $R_i$  at 1.0 as the necessary and sufficient condition for stability, considering nonlinear interactions in the flow, which means for  $0.25 < R_i < 1.0$ , turbulence is allowed. For  $R_i > 1$ , the fluid is generally considered stable (Silva et al., 1999; Galperin et al., 2007).

## 2.4 Model Domain and Grid

The model domain is from 56°W to 53°W and 45.5°N to 47.8°N (Fig. 2-1). The geometry of the domain includes Placentia Bay and some coastal ocean banks such as Green Bank, Whale Bank and St. Pierre Bank. The Avalon Channel lies between Whale Bank and Burin Peninsula; the Haddock Channel is sited between Whale Bank and Green Bank. The unstructured triangular grid was designed using the SMS grid generator software ([www.aquaveo.com/software/sms-learning](http://www.aquaveo.com/software/sms-learning)) (Fig. 2-2). The grid resolution is most coarse along the open boundary (3-5km) and finest along the coastlines (200m). The total number of model nodes and elements are 25414 and 47629. The node number on model lateral open boundary is 171. There are  $kb=31$  unequally geometric sigma levels in the vertical specified as  $\sigma(k) = [(k - 1)/(kb - 1)]^2$ , where  $k$  varies from 1 to  $kb$ . Thus, there is a minimum spacing within 0.2m near the sea surface and the seabed to resolve the shear current and thermodynamic process there. The model bathymetry is mainly derived from the high-resolution, multi-beam bathymetry of the Canadian Hydrographic Service. To minimize the pressure gradient errors (Mellor et al., 1993), the bathymetry was smoothed using the same method as in Ma et al. (2012).

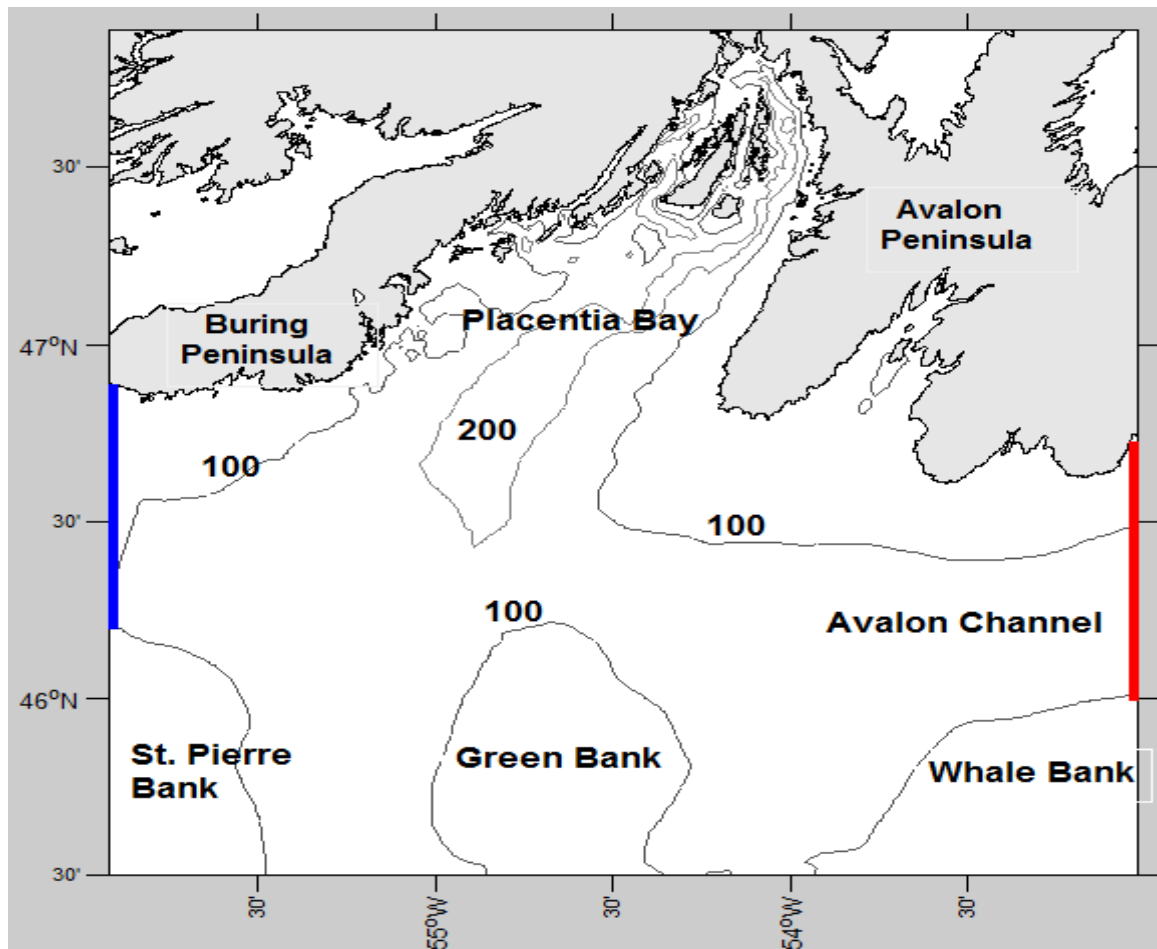


Fig 2-1: Map of model domain showing the major locations, features and bathymetry (100m and 200m contours). The bathymetry data is from ETOP5. The red and blue lines represent selected transects at east and west open boundary.

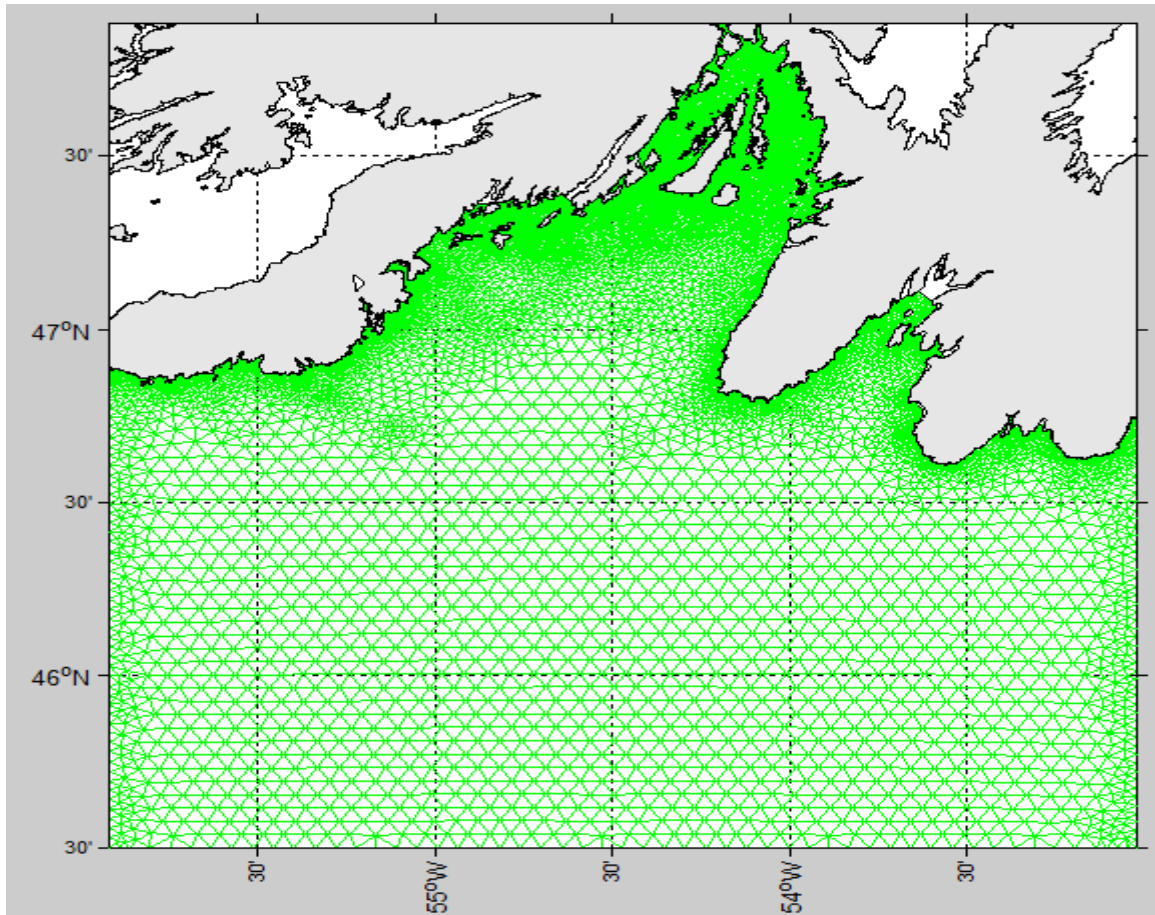


Fig 2-2: The horizontal grid used in this thesis comprised of 25414 nodes and 47629 elements.

## 2.5 Model Surface Forcing

In this thesis, the model was forced by spatially and temporally changing winds and heat fluxes at the sea surface for the whole domain and time integration. Air pressure and surface precipitation/evaporation were not included in this study.

The wind and heat flux fields are interpolated onto the entire model grid from the NCEP North American Regional Reanalysis (NARR) atmospheric forcing dataset ([www.esrl.noaa.gov/psd](http://www.esrl.noaa.gov/psd), Mesinger et al., 2006). The NARR project is an extension of the NCEP Global Reanalysis that is run over North America Region. The NARR model uses NCEP Eta Model with very high resolution ( $349 \times 277$ , the resolution is 0.3 degrees at the lowest latitude) together with the Regional Data Assimilation System (RDAS). The NARR datasets include eight times daily (three-hourly) data of many variables at fixed levels or subsurface from 1979 to present.

For the input file of wind fields, three-hourly eastward wind speed  $U$  and northward wind speed  $V$  at 10 meters height are extracted and interpolated onto all grid elements. For the input file of heat flux fields, three-hourly surface net heat fluxes and short wave radiations are extracted and interpolated onto all grid nodes. The surface net heat fluxes are calculated with the addition of six variables from NARR, which are the Downward Longwave Radiation Flux (positive), Upward Longwave Radiation Flux (negative), Downward Shortwave Radiation Flux (positive), Upward Shortwave Radiation Flux (negative), Sensible Heat Flux (negative) and Latent Heat Flux (negative). The short wave radiation is the addition of Downward Shortwave Radiation Flux (positive) and Upward Shortwave Radiation Flux (negative). For the model domain of this thesis, there

are 74 data grid nodes located, which could generally describe the spatial variability of the winds and heat fluxes in this area. The NARR winds and net heat flux are interpolated onto locations of several buoys to inspect their spatial distribution and temporal variation (Fig. 2-3 and Fig. 2-4).

In Fig. 2-3, the spatial distribution of the monthly-mean NARR winds over Placentia Bay area was close to uniform most of the time, which means it can be represented by only one wind vector when plotted in the figures of horizontal distribution of surface circulation. The interannual variabilities of the monthly-mean NARR winds were not obvious at most of the months except Dec. The monthly-mean wind direction on Dec 2010 has a westward component with amplitude of about  $3.0 \text{ m/s}$ , while the monthly-mean wind direction on the other three Dec all had eastward component with amplitude of approximately  $2.5 \text{ m/s}$ ,  $2.0 \text{ m/s}$  and  $2.5 \text{ m/s}$ .

In Fig. 2-4, the spatial distribution of the monthly-mean NARR net heat flux over Placentia Bay area was close to uniform most of the time. The monthly-mean NARR net heat flux showed relatively strong interannual variabilities at some months, such as: the net heat flux on Dec 2010 was only about  $50 \text{ W/m}^2$ , but up to about  $150 \text{ W/m}^2$  on Dec 2013; the net heat flux on Nov 2014 was only about  $75 \text{ W/m}^2$ , but up to about  $170 \text{ W/m}^2$  on Nov 2010; the net heat flux on Jan 2012 was only about  $75 \text{ W/m}^2$ , but up to about  $150 \text{ W/m}^2$  on Jan 2013.

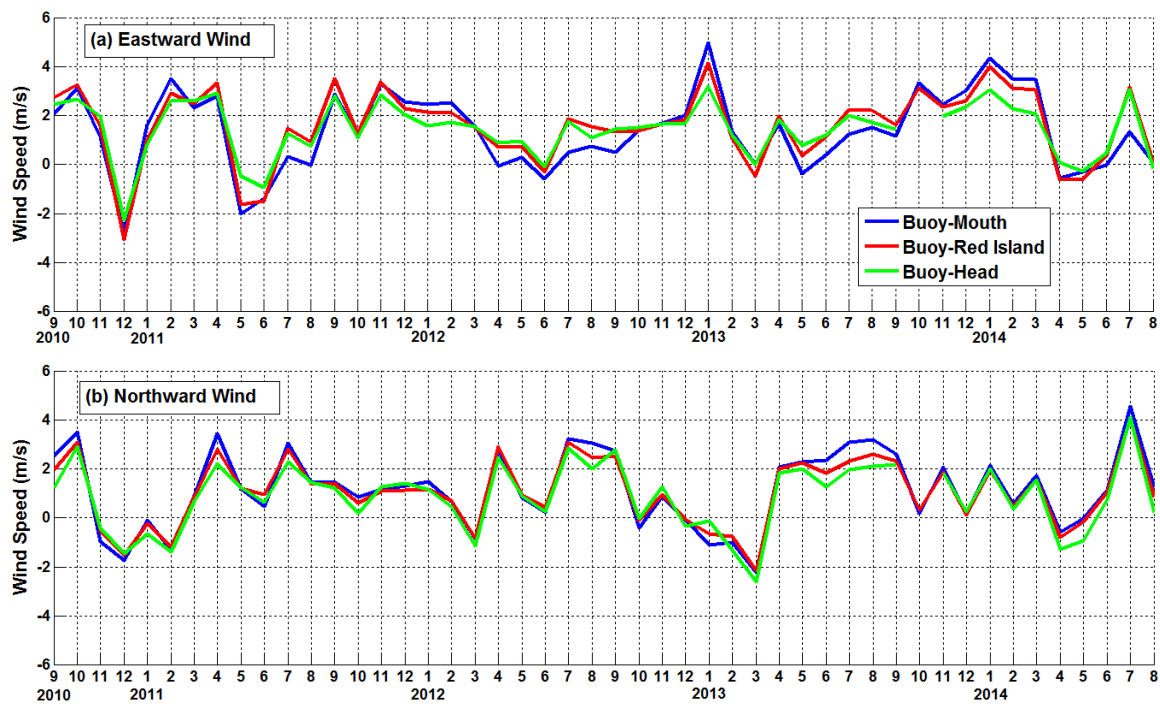


Fig 2-3: Monthly-mean NARR wind speed at 10m high over the sea surface: (a) eastward wind; (b) northward wind. The blue, red and green lines represent NARR wind interpolated onto locations at Buoy-Mouth, Buoy-Red Islands and Buoy-Head.

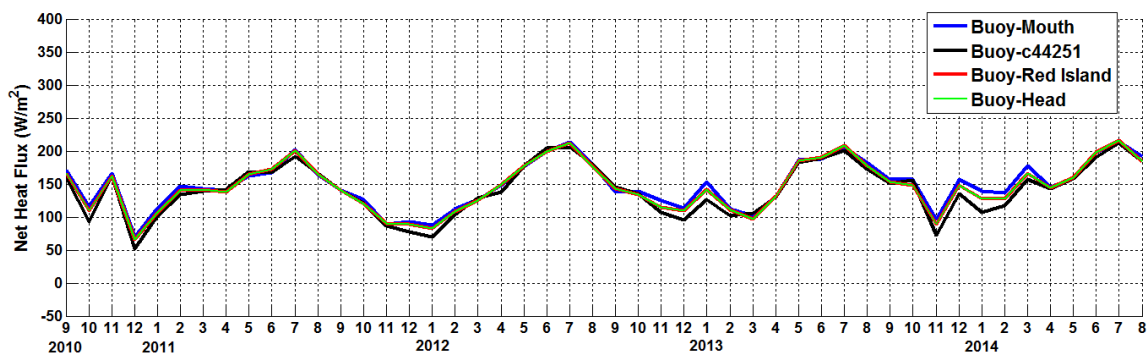


Fig 2-4: Monthly-mean NARR net heat flux at sea surface. The blue, red, green and black lines represent NARR net heat flux interpolated onto locations at Buoy-Mouth, Buoy-Red Islands, Buoy-Head and Buoy-c44251.

## 2.6 Open Boundary Conditions

Five leading semi-diurnal and diurnal tidal constituents ( $M_2, S_2, N_2, K_1, O_1$ ) are obtained from a regional model (Ma et al., 2015) and specified along the open boundary. Note that this shelf model reproduces tidal elevations accurately.

For non-tidal sea level, temperature and salinity on the open boundary, Ma et al. (2012) and Ma (2015) both interpolated output from large-scale Newfoundland Shelf models (Han et al., 2011; Ma et al., 2015). However, neither of these two shelf models had durations longer than 1 year, thus, can be used for the longer term simulations. In this thesis, output of non-tidal sea level, temperature and salinity from a near real time global ocean prediction system are interpolated to provide open boundary forcing.

The global prediction system and its experiments are based on HYbrid Coordinate Ocean Model (HYCOM 2.2) and the Navy Coupled Ocean Data Assimilation (NCODA) system and operated by the Naval Research Laboratory, from 2008 to present (<http://hycom.org/dataserver/glb-analysis> GLBa0.08: expt\_90.6, expt\_90.8, expt\_90.9, expt\_91.0, expt\_91.1.). Computations are carried out on a Mercator grid between 78°S and 47°N (1/12° equatorial resolution). The horizontal dimensions of the global grid are 4500 × 3298 grid points resulting in ~7 km spacing on average, together with 32 vertical layers ranged from 0 to 5500 m. Daily output of non-tidal sea level is provided, together with temperature and salinity at 32 vertical layers.

The output from these experiments has spatial coverage of 60×63 grid points in the domain of this thesis, concentrated mainly in the outer bay area. For the maximum depth on the open boundary is 152 m, temperature and salinity at the first ten vertical levels (0

m, 10 m, 20 m, 30 m, 50 m, 75 m, 100 m, 125 m, 150 m, 200 m) and non-tidal sea level during Aug 1, 2010 and Aug 31, 2014 are extracted for interpolation. During the interpolation of non-tidal sea level, NaN (Not a Number) data at some nodes close to the coastline are replaced by values at nearest nodes. During the interpolation of temperature and salinity, data at the first ten vertical levels from HYCOM horizontal grid are firstly interpolated horizontally onto the same levels at the open boundary. NaN data are replaced by values at nearest nodes at the same depth; then the obtained fields are interpolated again vertically onto 30 sigma levels.

A sponge layer is usually specified around the model domain with a damping zone weighted from the open boundary into the interior with a specified radius of influence to ensure that the radiation condition will also suppress the noise perturbation wave energy reflected back into the computational domain. This method works for the application of FVCOM to the Gulf of Maine/Georges Bank region and has shown to be stable for long-time integrations (seasonal to years). In this thesis, the influence radius and the damping coefficient of each open boundary nodes are 20000 *m* and 0.0001, respectively.

## **2.7 Additional Empirical Transport on the Open Boundary**

Because the general circulation around Placentia Bay is strongly influenced by the westward inshore branch of the Labrador Currents flowing through Avalon Channel and extended coastal area (Petrie and Anderson, 1983; Hart et al., 1999; Schillinger et al., 2000; Ma et al., 2012), the monthly-mean transport calculated from HYCOM on the eastern open boundary along the Avalon Channel and extended coastal area needs to be compared with previous model results to see its relationship with the real transport from

the inshore branch of Labrador Current. The first step in doing this was to extract eastward currents at the first eight levels (0m, 10m, 20m, 30m, 50m, 75m, 100m, 125m) from Sep 1, 2010 to Aug 31, 2014 by interpolating to a selected east open boundary from coast to the offshore bound of Avalon Channel (the red line in Fig 1-1). The interpolated current at each level and each open boundary node is treated as average currents for vertical layers between each level and for horizontal distance between each open boundary node. Then the transport on the selected east open boundary could be calculated by adding transport of each layer and distance together.

Han et al. (2008, Fig-14d) presented that the annual mean transport through Avalon Channel (inshore of the 90m isobath) is 0.7 Sv (with a peak transport of 1.2 Sv in November), and its monthly variability has only one biggest value in November (1.2 Sv) and then falls down to reach the smallest value in July; while, according to the calculation of transport on the selected eastern open boundary from HYCOM (dotted line in Fig 2-5), the annual mean transport through Avalon Channel (inshore of the 100m isobath) is about 0.4 Sv, and its monthly variability is greatest in November (0.8 Sv) and then falls down to reach the smallest value in May. Han et al. (2011) stated that the mean transport through Avalon Channel (inshore of the 100m isobaths) during the spring and fall of 1999 was 0.8 Sv, compared with about 0.4 Sv during spring and fall from HYCOM.

On the basis of the above comparisons, it suggests that the transport calculation on the selected eastern open boundary from HYCOM has similar seasonal variability with previous model results, but underestimate the transport from the inshore branch of Labrador Current. Thus, in this thesis, an additional empirical inflow with a time-independent value of 0.5 Sv is added on the selected east open boundary (the red line in

Fig 2-1). To ensure the conservation of the kinetic energy, an additional outflow with a constant value 0.5 Sv is added on the selected west open boundary (the blue line in Fig 2-1) with a linear distribution. The additional transports are added in the form of sea level slope on the selected open boundary under the geostrophic assumption (Cushman-Roisin and Beckers, 2011). The added offshore sea level slope (highest at the coast) for the inflow on the selected east open boundary has an asymmetric parabolic distribution, with the most inflow concentrated in Avalon Channel (Fig 2-6), while, the added sea level slope for the outflow has uniform distributions .

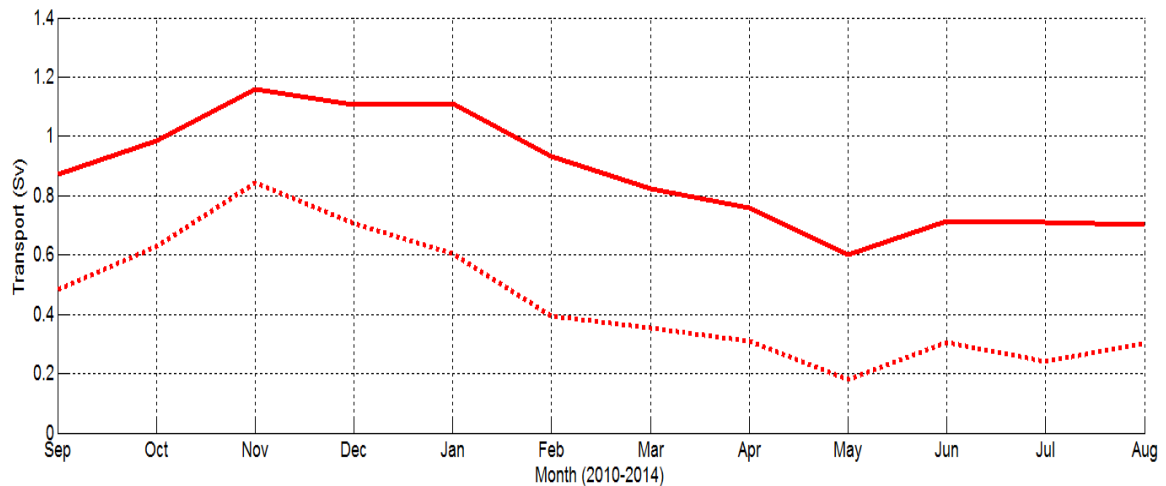


Fig 2-5: Monthly-mean transport on selected east open boundary according to HYCOM output (dotted line) and Monthly-mean transport on selected east open boundary according to FVCOM output (solid line). Positive sign means westward direction.

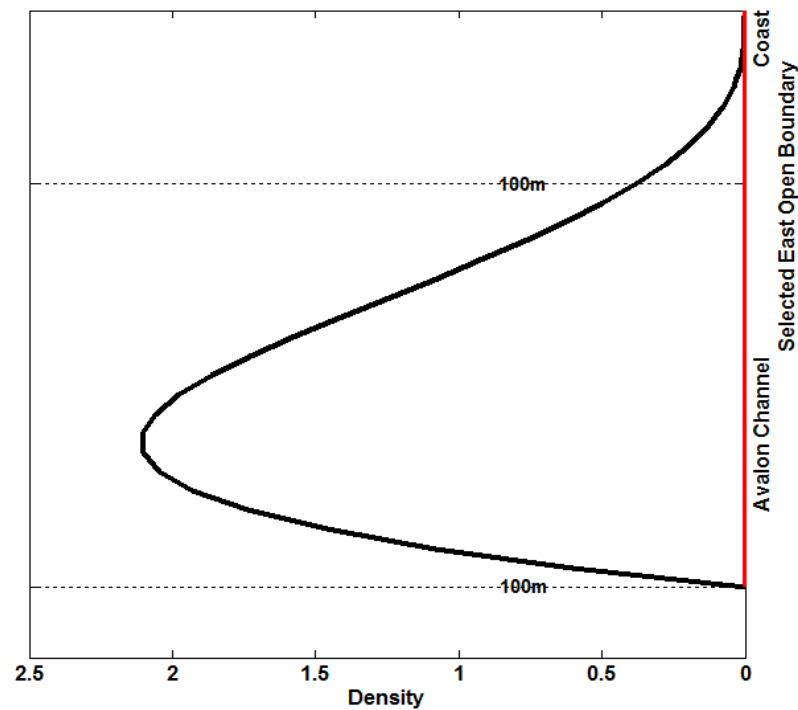


Fig 2-6: Map showing the Probability Density Function (black line) of the added asymmetric parabolic sea level slope on the selected east open boundary (red line), with the most slope in Avalon Channel. The dotted lines are 100m contour line.

## 2.8 Initial Conditions

The initial temperature and salinity conditions on all nodes at each sigma level are interpolated from the climatological monthly-mean temperature and salinity data (Geshelin et al., 1999) at standard z-level depths (0,10,-20,-30,-50,-75,-100,-125,-150,-200,-250,-300,-400,-500,-600,-700,800,-900,-1000,-1100,-1200,-1300,-1400,-1500,-1750,-2000,-2500,3000,-3500,-4000,-4500m). The model then has to spin up from rest.

The initial current velocities and sea surface elevations are both set to zero, which means the whole water body of the domain is still.

## 2.9 Model Runs and Parameterization

In this thesis, a three dimensional, prognostic and baroclinic model based on FVCOM is developed. Restricted by the CFL condition, the external time step is 0.5 s and the internal time step is 5 s. The surface wind forcing and heat flux are applied three-hourly without any nudging scheme, while non-tidal sea level, temperature and salinity interpolated from HYCOM output at the open boundary are applied daily without any nudging scheme. In addition, empirical offshore sea level slopes are added on the selected west and east open boundary. No normal flow is applied at the lateral solid boundaries. Instead of the default Mellor-Yamada level 2.5 turbulent closure, the second-order  $k - \varepsilon$  turbulent closure from General Ocean Turbulence Model (GOTM; available at <http://www.gotm.net>) is used here. Considering that there is typically no ice formation during the winter around Placentia Bay, the lower limit of the evolved water temperature is controlled to not colder than  $-1.9^{\circ}\text{C}$ , which is close to the freezing point of sea water.

The model is started cold (that is from rest) and run from August 1, 2010 to Aug 31, 2014. The model output includes three-dimensional horizontal velocity, vertical averaged horizontal velocity, sea level, temperature and salinity. According to Ma et al. (2012), 19 days is long enough to spin up the model for realistic forcing of Placentia Bay with initial elevation and velocity fields generated from a shelf model. Considering the complete “coldstart” from a still ocean in this thesis, model results for the first month are discarded, and outputs after Sep 1, 2010 are validated and discussed with the duration of the whole four years. For the convenience to validate the simulated results with observations, the whole four-year duration is separated into four independent time interval, each with one

year duration: Sep 1, 2010~Aug 31, 2011; Sep 1, 2011~Aug 31, 2012; Sep 1, 2012~Aug 31, 2013; Sep 1, 2013~Aug 31, 2014, which are named in this thesis as 2010-2011, 2011-2012, 2012-2013 and 2013-2014.

### **3. Observational Data**

#### **3.1 Observations of Meteorological Stations**

There are two Environmental Canada's meteorological stations observing tides, water levels and weather conditions in Placentia Bay, one is Argentia Station (Station#835) located on eastern side of the middle bay, the other is St. Lawrence Station (Station#755) located on the western side of the outer bay. (See the red diamonds in Figure 1-1)

In this thesis, hourly sea level data during Sep 1, 2010 and Aug 31, 2014 at these two stations are downloaded from Tides and Water Levels Data Archive of Fisheries and Oceans Canada in meters at local standard time (LST). Then the T\_Tide Matlab toolbox (Pawlowicz et al., 2002) is used to separate major tidal elevations and non-tidal elevations through harmonic analysis method. For data analysis and further comparison, hourly wind speed/direction data at 10m and hourly air pressure data at local standard time (LST) during Sep 1, 2010 and Aug 31, 2014 are also downloaded at these two stations from Historical Climate Data Archive of Environment Canada, the latter of which are used to remove the inverse barometric effect. Note that the measured wind direction is from the true north.

During the selected period, there are some consecutive time intervals when the observations were not available at Argentia station, such as Apr 11~Apr 29, 2013; Jun 27~Jul 8, 2013; Dec 14, 2013~Mar 10, 2014. At St. Lawrence station, observations were not available during Oct 29~Nov 9, 2011; Feb 7~Feb 10, 2014.

### 3.2 Observations of Mooring Buoys

The three meteorological/oceanographic buoys were deployed by the Marine Institute of Memorial University (<http://www.smartbay.ca/>) in Placentia Bay to provide near-real time atmospheric and coastal ocean surface conditions, including wind vectors, SST, sea surface salinity, current vectors and wave information etc. (See magenta dots: Buoy-Mouth, Buoy-Red Island and Buoy-Head in Figure 1-1). The first buoy (Buoy-Mouth) has been deployed at the mouth of Placentia Bay in a water depth of about **230m** since August 18, 2006; the second one (Buoy-Red Island) is positioned at the Pilot Boarding Station for Placentia Bay near Argentia in a water depth of about **153m** since July 6, 2010; the third one (Buoy-Head) was originally located at the head of Placentia Bay in a water depth of about **43 m** at Latitude 47° 47.4' N, Longitude 54° 02.9' W during July 21, 2010 and Oct 10, 2013, and has been relocated off the coast to Latitude 47° 45.5' N, Longitude 54° 04.5' W since October 11, 2013, in a water depth of about **115 m**. In this thesis, half-hourly wind vectors, air temperature, SST, surface currents with UTC time format at all three buoys are downloaded during Sep 1, 2010 and Aug 31, 2014 for further analysis and comparisons. Note that the measured current direction is toward magnetic north, while the measured wind direction is from magnetic north.

During the selected period, there are some consecutive time intervals when the observations were not available at Buoy-Mouth, such as Mar 9~Jun 26, 2012 for both SST and surface currents. As for Buoy-Red Island, SST were not available during Sep 1, 2010~Jan 17, 2011; Nov 9, 2011~Jun 26, 2012; Jan 1~Jan 30, 2013, while, surface currents were not available for the periods Nov 9, 2011~Jun 26, 2012; Jan 1~Jan 30,

2013. As for Buoy-Head, SST were not available during Sep 1, 2010~Jan 17, 2012; Jun 7~Sep 23, 2011; Mar 5~May 2, 2014, while, surface currents were not available during Jun 7~Sep 23, 2011; Mar 5~May 2, 2014; Aug 2~Aug 31, 2014.

There is also a weather buoy positioned at Nickerson Bank outside Placentia Bay off Avalon Peninsula (See magenta dot: Buoy-c44251 in Figure 1-1), measuring waves, SST and atmospheric conditions, in a depth of about 80 m (Data can be downloaded from *Waves and other Moored Marine Buoy Observations Archive* of Fisheries and Oceans Canada). In this thesis, only hourly SST with UTC time format are extracted for further analysis and comparison during Sep 1, 2010 and Aug 31, 2014. During the selected period, there are some consecutive time intervals when the observations were not available at Buoy-c44251, such as Nov 13, 2011~May 16, 2012; Jul 14~Oct 11, 2012.

### **3.2.1 Wind and Surface current Observations**

The monthly-mean wind vectors (at 4.2 m high), eastward surface currents  $u$  and northward surface currents  $v$  (at 0.5 m depth) at three meteorological/oceanographic buoys are plotted in Figure 3-1 (no data or bad data at some months). According to surface Ekman layer theory (e.g. Cushman-Roisin and Beckers., 2011), the wind induced surface current is oriented  $45^\circ$  to the wind stress (right in the northern hemisphere), several big variabilities existed in Figure 3-1a and Figure 3-1b can be partially due to large local wind speed or obvious wind direction change in Figure 3-1c.

At the Buoy-mouth (blue lines), observed  $u$  and  $v$  are all negative, indicating a general southwestward surface currents. A sharp negative increase of  $u$  from Sep 2012 to Oct 2012 may be related to a big wind direction change from northeastward to

southeastward; a consecutive negative decreasing of  $u$  from May 2014 to Jul 2014 may be induced firstly by a big wind direction change from southwestward to northeastward, and then, followed by an intensification of the northeastward wind; two negative peak values of  $v$  at Feb 2011 and Jan 2013 may be due to intensified southeastward winds.

At the buoy-red islands, the observed  $v$  is negative at most time, but  $u$  is shifted around zero. A sharp negative decrease of  $v$  until near-positive zero from Mar 2011 to May 2011 may be related to big wind direction changes from eastward to northeastward and then southwestward.

At the buoy-head, both observed  $u$  and  $v$  have very small amplitudes ( $<0.04m/s$ ), except for a negative peak of  $v$  at Jan 2013 which may be due to intensified southeastward winds.

### **3.2.2 Air temperature and SST Observations**

The monthly-mean SST at 0.5m depth for all four buoys (including the weather Buoy-c44251) and air temperature at 3.5m high only for three meteorological buoys are plotted in Figure 3-2 and Figure 3-3 (no data or bad data at some months).

The SST in Figure 3-2 shows similar seasonal variability but different interannual variability. The hottest SST was observed on Aug 2012 while the coolest SST occurred in Sep 2011; the coldest SST happened on Mar 2014, while the warmest SST occurred in Mar 2011. The hottest SST at Buoy-head seems higher than that at Buoy-mouth and Buoy-red islands in summer 2012 and summer 2013. The Buoy-44251 in the outer area of Placentia Bay has higher SST in winter 2013 and winter 2014 than the other three buoys.

The variability of SST at three meteorological buoys is directly proportional to the

related variabilities of air temperature (Figure 3-3).

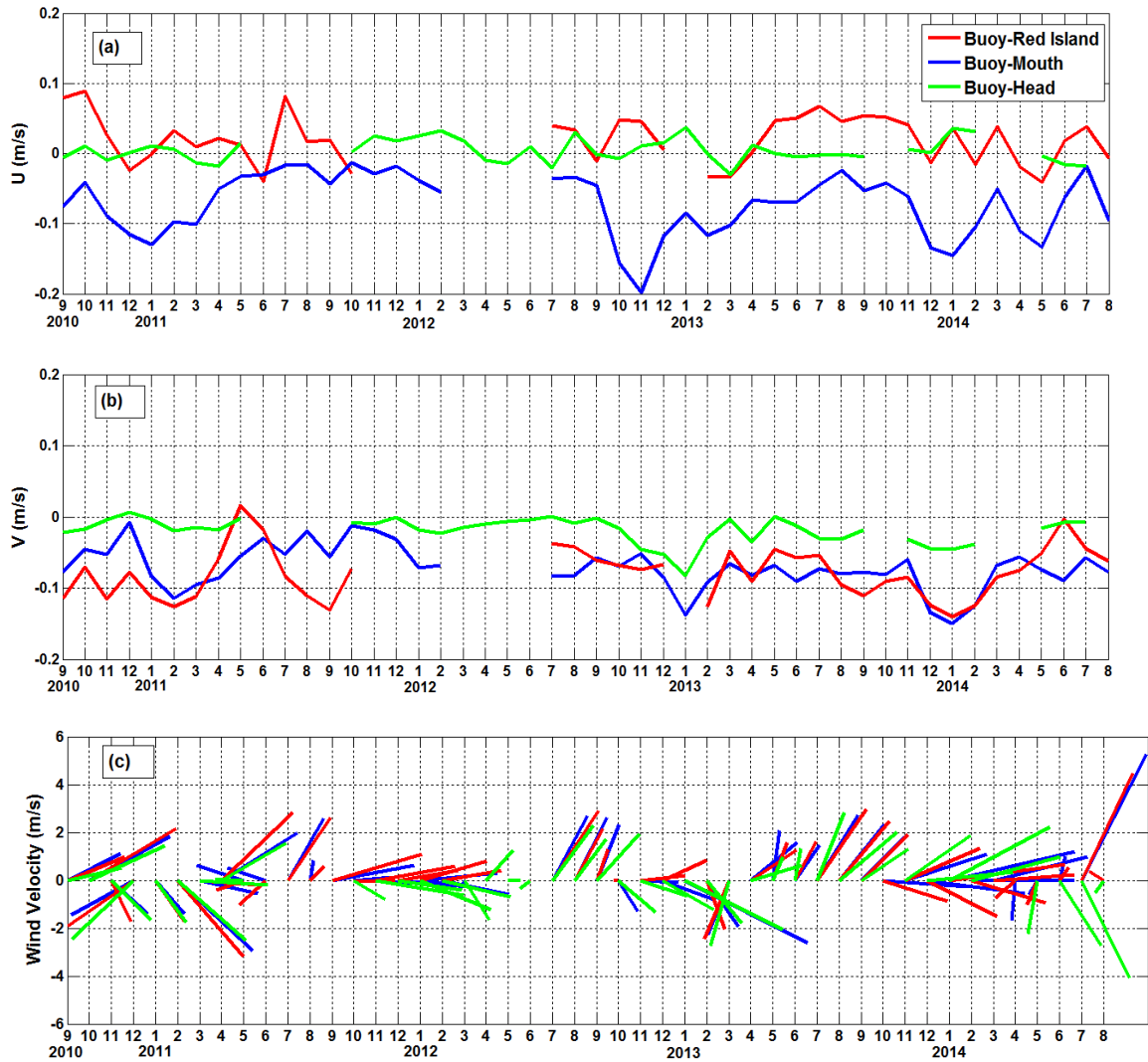


Fig 3-1: Monthly-mean observed (a) surface eastward current velocity  $U$ , (b) surface northward current velocity  $V$ , and (c) surface wind velocity at three buoys from Sep 2010 to Aug 2014. The blue, red and green lines represent data at Buoy-Mouth, Buoy-Red Island and Buoy-Head.

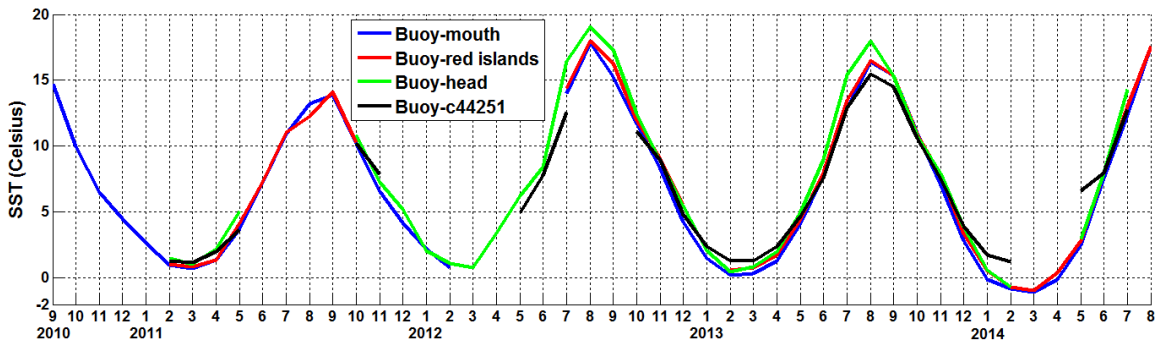


Fig 3-2: Monthly-mean SST at four buoys from Sep 2010 to Aug 2014. The blue, red, green and black lines represent data at Buoy-Mouth, Buoy-Red Islands, Buoy-Head and Buoy-c44251.

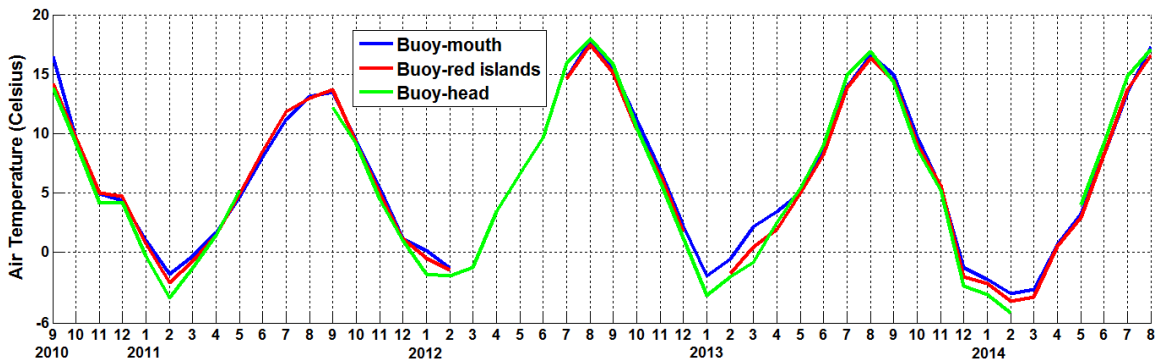


Fig 3-3: Monthly-mean Air Temperature at three buoys from Sep 2010 to Aug 2014. The blue, red and green lines represent data at Buoy-Mouth, Buoy-Red Islands and Buoy-Head.

## 4. Model Validation

### 4.1 Data Analysis Method

To evaluate the model solutions qualitatively and quantitatively, various moored measurement data are compared with model results. For low-frequency comparisons, the six-hourly outputs are directly averaged to monthly-mean and no low-pass filter needs to be applied. It should be noted that if the percentage of the missing data in one month reaches 40%, the related observational monthly-mean data is discarded.

Five primary goodness-of-fit indices are used here for model validation of water levels, currents and temperature. The first measure of agreement is the root-mean-square difference (RMSD):

$$RMSD = \sqrt{\frac{\sum(O-M)^2}{numel(M)}} \quad (4.1)$$

where  $O$  and  $M$  represent observations and corresponding model calculated values.  $numel(M)$  is the total number of compared points. Lower RMSD values mean better agreement. The best agreement occurs when the RMSD reaches zero.

The second measure of agreement is  $\gamma^2$  which is used to demonstrate the model's ability to simulate the variability of sea level anomalies, currents and temperature. It is defined as the ratio of the hindcast error variance to the observed variance:

$$\gamma^2 = \frac{Var(O-M)}{Var(O)} \quad (4.2)$$

where  $Var$  denotes variance. A small  $\gamma^2$  indicated better agreement between the observed and simulated values. If their difference results in a value of  $Var(O - M)$  greater than

$Var(O)$ , the  $\gamma^2$  can be greater than unity. It should be noted that  $\gamma^2$  does not take into account the model's bias and could be small due to strong observed variance.

The third measure of agreement is the speed difference ratio ( $SDR$ ) defined as the ratio of the sum of the squared speed difference to the sum of the squared magnitudes of the observed velocities, that is,

$$SDR = \sum (|V_m| - |V_o|)^2 / \sum |V_o|^2 \quad (4.3)$$

The fourth measure of agreement is to examine the velocity difference ratio ( $VDR$ ) defined as the ratio of the sum of the squared magnitudes of the vector velocity differences to the sum of the squared magnitudes of the observed velocities, that is,

$$VDR = \sum |V_m - V_o|^2 / \sum |V_o|^2 \quad (4.4)$$

where  $V_m$  is the horizontal model velocity and  $V_o$  is the horizontal observational velocity. Lower  $VDR$  values indicate better agreement, with  $VDR=0$  indicating exact agreement. The  $VDR$  values, representing a relative error that takes into account the simulated and observed values in both magnitude and direction, are generally greater than  $SDR$ .

The last measure of agreement is the correlation coefficient between the simulated and observed time-series values.

## 4.2 Validation of Tidal Elevation

In order to validate tidal information with tide gauge observations and previous model results (Ma, 2015 Chapter 4), harmonic analysis including the five leading  $M_2, S_2, N_2, K_1, O_1$  constituents is used to extract tidal elevation during Sep 1, 2010 and Aug 31, 2011 from the model solution with one-hourly output.

The horizontal distribution (not shown) of  $M_2$  shows an increasing trend in amplitude towards the head of bay. For  $K_1$ , the amplitude decreases towards the western side of bay, a result that is consistent with previous model and observation results (Han et al., 2010; Ma et al., 2012). Details of the horizontal tidal distribution can be found in Ma et al. (2012). The tidal elevations observed at Argentia Station and Tacks Beach Station (see Ma et al. 2012, Fig. 4-1, location D) are compared with model interpolated results. The detailed statistics are calculated in Table 4-1. The RMSD in the present study are within 2.3 cm in amplitude, and within  $6.3^\circ$  except  $K_1$  in phase. The statistics from Ma (2015 Chapter 4.4) is also listed in Table 4-1. With the same tidal constants set on the open boundary but a longer run than Ma (2015 Chapter 4.4), the current solution shows improvement in reproducing semi-diurnal constituents.

Table 4-1: Summary and statistics for observed and computed semi-diurnal and diurnal tidal elevations at coastal tide-gauge stations. Observational locations were shown in Ma (2015)

	$M_2$		$S_2$		$N_2$	
	Ma (2015)	Current Study	Ma (2015)	Current Study	Ma (2015)	Current Study
$RMS_{amp}$ (cm)	2.5	2.3	1.2	0.8	1.4	1.3
$RMS_{phase}$ ( $^{\circ}$ )	4.9	4.5	5.8	4.0	2.3	2.2
	$K_1$		$O_1$			
	Ma (2015)	Current Study	Ma (2015)	Current Study		
$RMS_{amp}$ (cm)	1.0	1.1	1.8	0.9		
$RMS_{phase}$ ( $^{\circ}$ )	12.4	13.0	3.6	6.3		

### 4.3 Evaluation of Monthly-mean Water Levels

Six-hourly simulated water levels during Sep 1, 2010 and Aug 31, 2014 are interpolated onto the Argentia and St. Lawrence Stations (See tide gauge locations in Fig 1-1) and then averaged to provide 48 monthly-mean water levels at both sites. In the present study, the inverse barometric effect is not included in the model momentum equations. Thus, before averaging hourly tide gauge water level observations to monthly-mean water levels for further comparison, the inverse barometric effect should be removed based on observed hourly atmospheric pressure at the same site. Finally, the simulated and observed sea level means are both removed to obtain comparisons of the simulated and observed monthly-mean sea level anomalies (Figure 4-1). (The monthly-mean observational values are NaN for Apr 2013, Dec 2013, Jan 2014 and Feb 2014 at the Argentia station because the percentage of the missing data during these months is higher than 40%)

The simulated sea level anomalies agree well with the observed ones, showing obvious similar seasonal and interannual variabilities at both tide gauge stations (Figure 4-1). The water levels are usually high in fall/winter and low in spring/summer. The largest peak happened in Oct 2013 at Argentia and Dec 2013 at St. Lawrence for the model but in Dec 2012 for the observations; the smallest peak happened both in Nov 2011 for the model and the observations; the largest trough happened in May 2013 for both the model and observations. At Argentia Station, the simulated sea level anomalies on Oct 2011/2012, Nov 2011/2012 and Dec 2011/2012 agreed very well with the observed ones and also showed distinct interannual variations in amplitude.

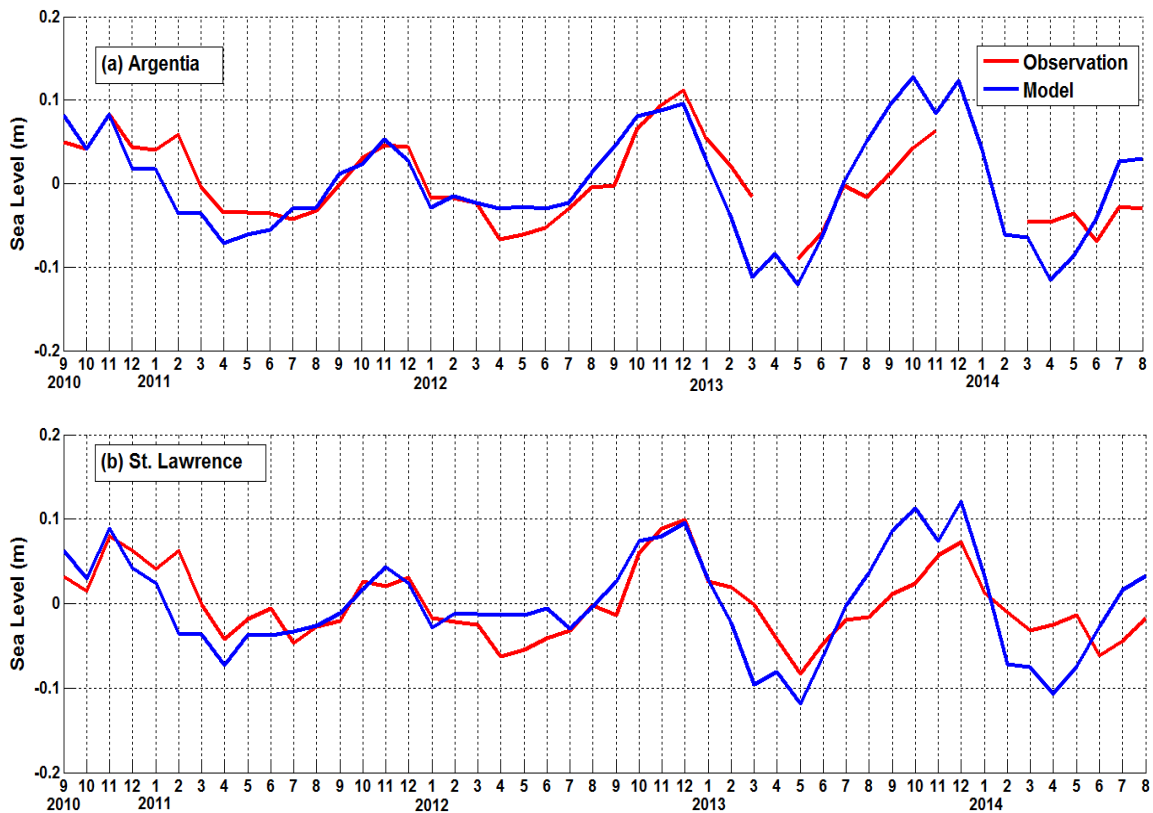


Fig. 4-1: Monthly-mean observed (red) and simulated (blue) sea level anomalies at (a) Argentina and (b) St. Lawrence during Sep 2010 and Aug 2014

Quantitative comparisons are also made between the model results and observations using monthly-mean sea level anomalies (Table 4-2). The largest annual sea level range is 24 cm in the model solutions and 20 cm in the observations. The averaged RMSD, correlation coefficients and  $\gamma^2$  between the observed and simulated monthly-mean sea level anomalies at tide gauge stations are 4 cm, 0.74 and 0.77 for the whole four years (2010-2014, 48 months), demonstrating good agreement for both magnitude and variability. For the interannual comparison, the smallest RMSD happened in 2011-2012 (2.1 cm averaged), while the largest RMSD occurred in 2013-2014 (5.6 cm averaged). All of the correlation coefficients in Table 4-2 are significant in 95% confidence interval.

There are at least two causes for the observed differences: (1) the surface wind forcing at tide gauge stations used in present model is interpolated from NARR datasets, which may be different from the local wind forcing observed directly at the tide gauge station both in amplitude and direction; (2) the accuracy of the transports defined at the open boundary of the model domain.

Table 4-2: Statistics from the comparison between observed and simulated monthly-mean sea level anomalies at two tide-gauge stations

Argentina Tide Gauge Station (Interannual Statistics)					
	2010-2011	2011-2012	2012-2013	2013-2014	Total
RMSD (cm)	3.5	1.8	4.4	5.7	4.0
Correlation	0.80	0.91	0.82	0.82	0.76
$\gamma^2$	0.49	0.20	0.53	1.61	0.69

St. Lawrence Tide Gauge Station (Interannual Statistics)					
	2010-2011	2011-2012	2012-2013	2013-2014	Total
RMSD (cm)	3.4	2.4	4.2	5.5	4.0
Correlation	0.79	0.74	0.83	0.74	0.72
$\gamma^2$	0.46	0.46	0.61	1.53	0.84

#### 4.4 Evaluation of Monthly-mean Surface Currents

Six-hourly simulated eastward and northward currents for the first sigma layer on the surface during Sep 1, 2010 and Aug 31, 2014 are interpolated onto locations of Buoy-Mouth, Buoy-Red Island and Buoy-Head (See locations in Fig 3-1) and then averaged to get 48 monthly-mean currents to compare with the observational surface currents at 0.5m depth on each buoy-location (Fig. 4-2). The observed wind velocity at each buoy-location and the NARR wind velocity used as the input surface forcing of the model are also plotted in Fig. 4-2 to reveal their difference. The simulated surface currents at different sites are likely to have quite different dynamical characteristics. It should be noted that several monthly-mean observational values are NaN at each Buoy because the percentage of the missing data in these months is higher than 40%. Besides, the monthly-mean values in Oct 2013 at Buoy-head are discarded because the buoy changed its position during this month.

At Buoy-Mouth, both the simulated and observed surface currents are southwestward at most times probably due to the location at the mouth of the bay, where the strong influence of the remote water inflow from the westward inshore branch of Labrador Current can be felt, according to previous studies. The westward component (Fig 4-2a) is usually strong in fall/winter and weak in spring/summer. The strongest westward component occurred in Nov 2013 for the model but in Nov 2012 for the observations, while the weakest Nov happened in 2011 for both the model and the observation. At several months (mostly during summer) the simulated values became weakly eastward, while the observed ones were always directed westward. The southward

component (Fig 4-2b) is usually strong in winter, with the largest speed in Jan 2013 for model but in Jan 2014 for the observations. The weakest Jan happened in 2012 for both the model and the observation. At some months the simulated values underestimated the southward component, sometimes even became weakly northward, while the observed ones were always southward. It may be due to the difference between observed surface wind forcing at buoy site and model used surface wind forcing interpolated from NARR datasets (Fig 4-2c). For example, when the underestimate happened in Oct 2010 and Apr 2011, the NARR wind directions were both north to observed ones, which could partially strengthen northward current component or offset southward current component due to its relatively strong amplitudes. For several months, when the discrepancies were relatively large, such as in Oct 2012 and Oct 2013 for the eastward component, the accuracy of the transports defined at the open boundary of the model domain could be the key factor. Overall, the model reasonably captured the observational variability, direction and magnitude of the current vectors at Buoy-Mouth.

At Buoy-Red Island, the eastward velocities were mainly positive for both model and observation. The strongest eastward currents (Fig 4-2d) usually happened in summer and fall, when the wind direction was mainly northeastward (Fig 4-2f). However, the model overestimated the magnitude of the currents in eastward direction especially during summer, which may be partially due to the difference between observed and model used surface wind forcing. The observed and simulated northward components (Fig 4-2e) have obvious differences in both direction and magnitude. Generally the model overestimated the influence of the northward currents even when the observed and model used surface winds were very similar in both direction and magnitude, while the observed currents are

mainly directed southwards. Overall, at Buoy-Red Island the model reasonably captured the observational variability, direction and magnitude of the eastward components; however, a relative large discrepancy existed for the northward components.

At Buoy-Head, the original site was nearshore with a depth of about 43m, and then the buoy was moved offshore for about 4km on Oct 11, 2013, to a position with a depth of 115m (Fig 3-1). Thus, comparison needs to be separated at Oct 2013. Overall, the currents at Buoy-Head were relatively weak due to its location near the head of bay and its reduced influence from outside of the bay. Before Oct 2013, the model overestimated the magnitude of the eastward components (Fig 4-2g); meanwhile, the northward velocity was negative at most time, indicating southward currents, with partial influence from the surface wind forcing, such as Jan and Mar 2013. After Oct 2013, the simulated eastward velocities (Fig 4-2g) agree well with the observed ones; however, the simulated northward velocities (Fig 4-2h) showed big difference with the observed ones, especially in Jul 2014. It should be noted that there are also big difference in wind velocity during Jun and Jul 2014, but it is not enough to explain the current velocity changes at Buoy-Head after Oct 2013.

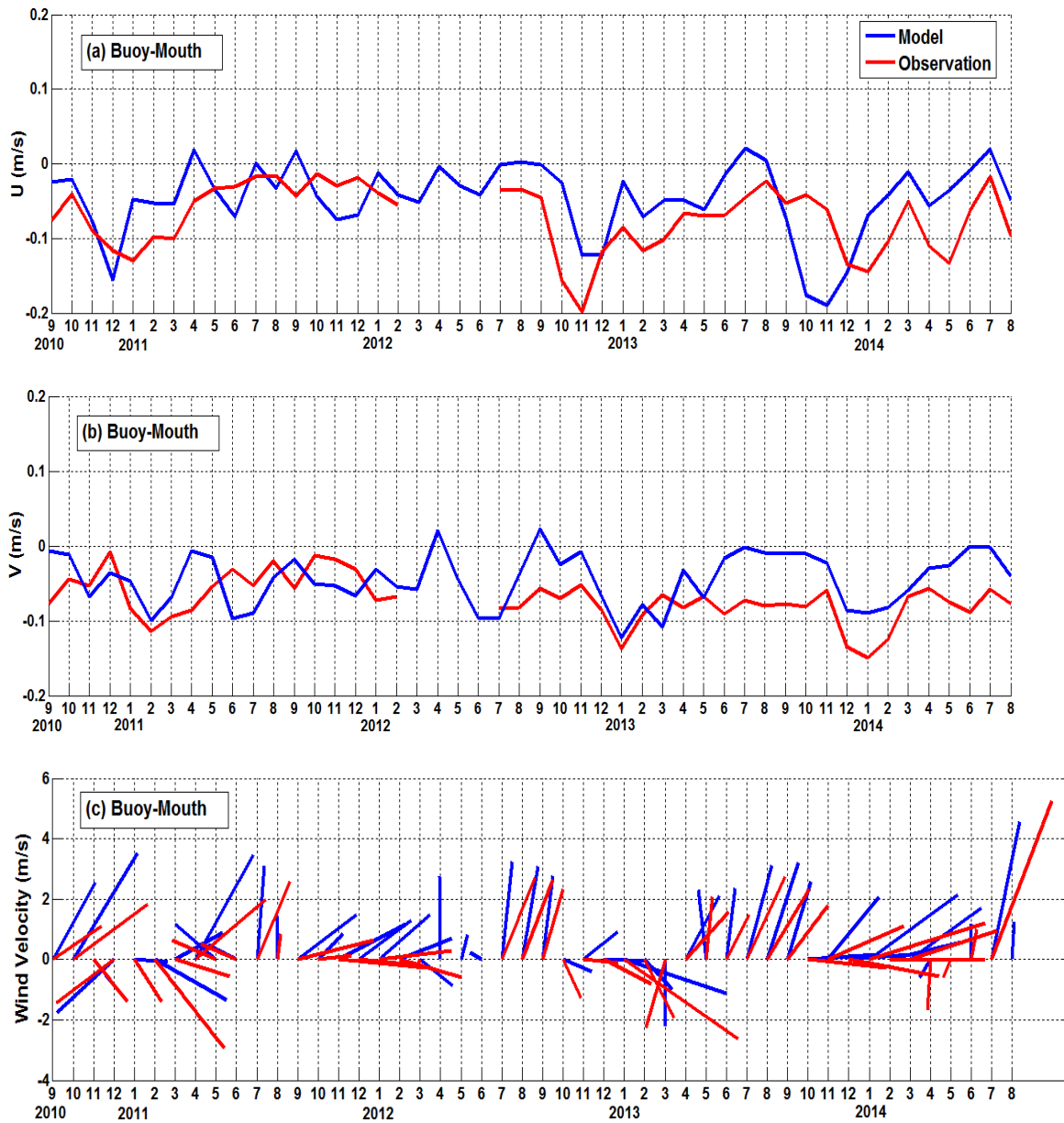


Fig. 4-2: Monthly-mean observed (red) and simulated (blue): surface eastward current velocity (U), surface northward current velocity (V) and surface wind velocity at (a)/(b)/(c) Buoy-Mouth; (c)/(d)/(e) Buoy-Red Islands; and (e)/(f)/(g) Buoy-Head.

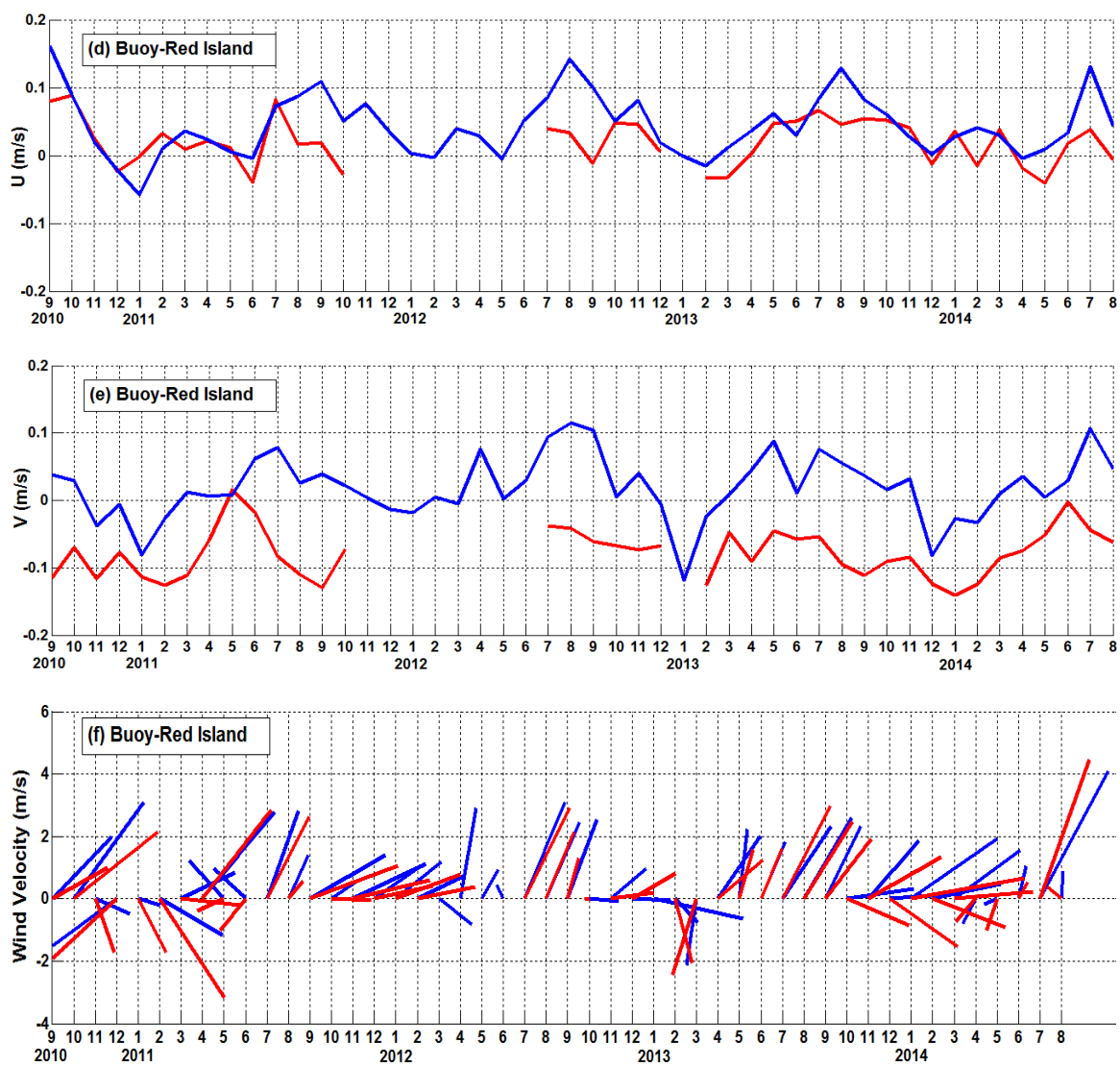


Fig 4-2 (continued)

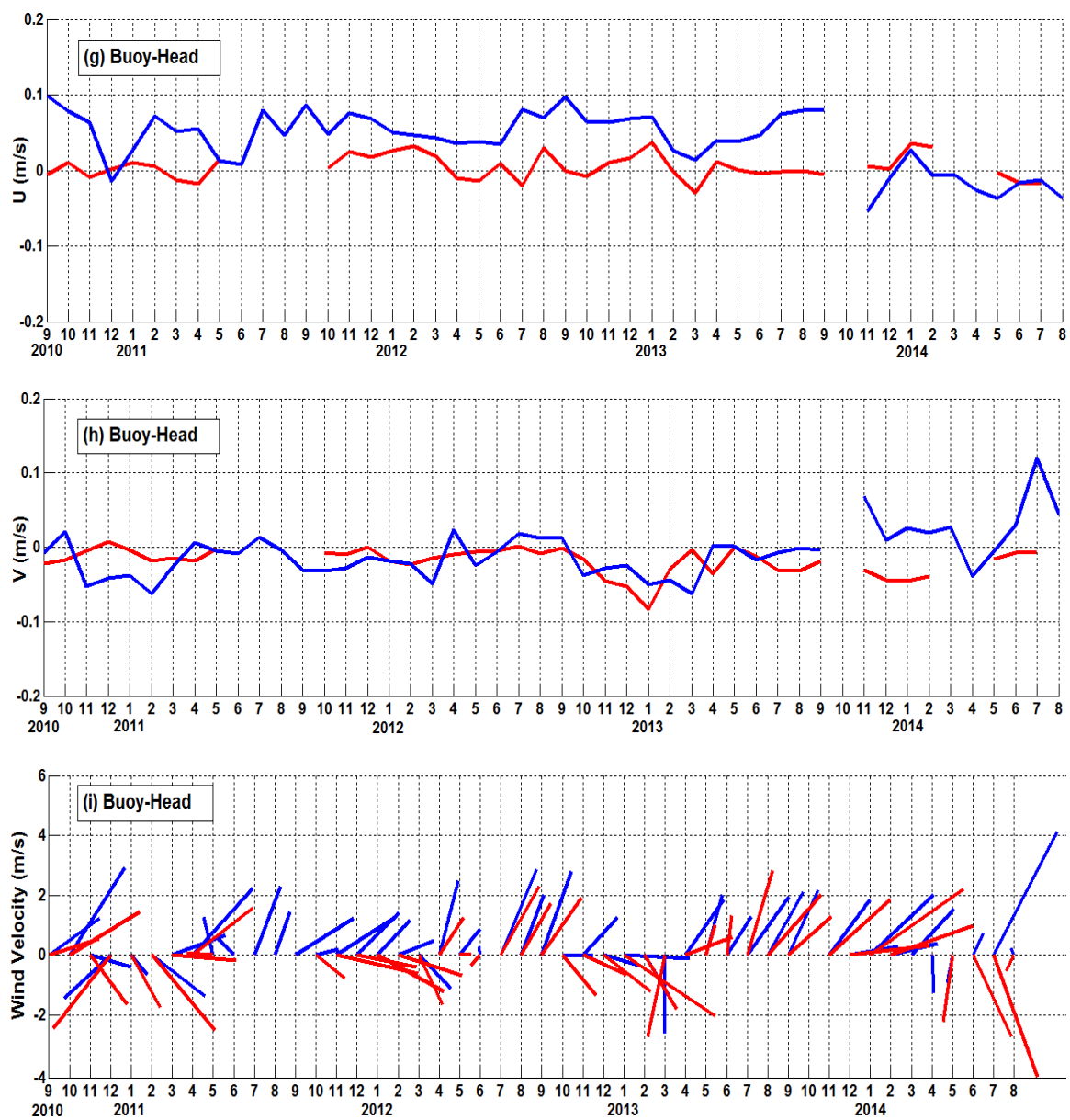


Fig 4-2 (continued)

Quantitative comparisons are also made between the model results and observations using monthly-mean eastward and northward surface currents at Buoy-Mouth (Table 4-3), Buoy-Red Island (Table 4-4) and Buoy-Head (Table 4-5). For the calculation of interannual statistics, if four or more NaNs exist in any one-year period (starting from Sep), "-" will be applied instead of real statistics. The correlation coefficients that are significant in 90% confidence interval in Table 4-3, Table 4-4 and Table 4-5 are highlighted in bold and underlined.

At Buoy-Mouth (Table 4-3), the RMSD and correlation coefficients for U/V in the whole four-year duration (2010-2014, 48 months) are 0.06/0.05 m/s and 0.40/0.30 (significant in 90% confidence interval), and the total SDR and VDR values are 0.29 and 0.42, indicating the well captured magnitude, direction for observed surface currents. For the interannual comparison, the VDR values are all less than 0.6, and statistics in 2012-2013 had the smallest SDR, VDR and better correlation (0.73) in east-westward direction, which captured the strongest increase in westward currents (Sep-Nov 2012), while statistics in 2013-2014 had the better correlation (0.79) in south-northward direction.

At Buoy-Red Island (Table 4-4), the RMSD and correlation coefficients for U/V in the whole four-year duration (2010-2014, 48 months) are 0.05/0.11 m/s and 0.60/0.50 (significant in 90% confidence interval), and the total SDR and VDR values are 0.36 and 1.62, demonstrating fairly good agreement in magnitude and variability between model and observations. For the interannual comparison, statistics in 2010-2011 had the smallest SDR, VDR and better correlation (0.76) in east-westward direction, which captured the large decrease in eastward currents (Oct-Nov 2010) and large increase in eastward

currents (Jun-Jul 2011), while statistics in 2011-2012 had the better correlation (0.71) in south-northward direction.

At Buoy-Head (Table 4-5), the RMSD and correlation coefficients for U/V in the whole four-year duration (2010-2014, 48 months) are 0.06/0.04 m/s and 0.01/0.01 (insignificant in 90% confidence interval), and the total SDR and VDR values are too large due to vary weak currents, showing limited ability to reproduce observational variability.

Table 4-3: Statistics from the comparison between observed and simulated monthly-mean surface currents (0.5m depth) at Buoy-Mouth

Buoy-Mouth (Interannual Statistics)					
	2010-2011	2011-2012	2012-2013	2013-2014	Total
RMSD-U (m/s)	0.04	0.04	0.06	0.07	0.06
RMSD-V (m/s)	0.04	0.03	0.05	0.05	0.05
Correlation-U	<b><u>0.55</u></b>	-0.44	<b><u>0.73</u></b>	0.09	<b><u>0.40</u></b>
Correlation-V	0.12	0.04	<b><u>0.59</u></b>	<b><u>0.78</u></b>	<b><u>0.30</u></b>
SDR	0.29	0.43	0.25	0.31	0.29
VDR	0.37	0.57	0.35	0.48	0.42

Table 4-4: Statistics from the comparison between observed and simulated monthly-mean surface currents (0.5m depth) at Buoy-Red Island

Buoy-Red Island (Interannual Statistics)					
	2010-2011	2011-2012	2012-2013	2013-2014	Total
RMSD-U (m/s)	0.04	0.08	0.05	0.04	0.05
RMSD-V (m/s)	0.10	0.14	0.11	0.10	0.11
Correlation-U	<b><u>0.76</u></b>	0.72	<b><u>0.57</u></b>	<b><u>0.59</u></b>	<b><u>0.60</u></b>
Correlation-V	0.37	0.71	0.41	<b><u>0.63</u></b>	<b><u>0.50</u></b>
SDR	0.22	0.77	0.37	0.40	0.36
VDR	1.12	3.67	2.11	1.30	1.62

Table 4-5: Statistics from the comparison between observed and simulated monthly-mean surface currents (0.5m depth) at Buoy-Head

Buoy-Head (Interannual Statistics)					
	2010-2011	2011-2012	2012-2013	2013-2014	Total
RMSD-U (m/s)	0.07	0.05	0.06	0.04	0.06
RMSD-V (m/s)	0.03	0.02	0.03	0.07	0.04
Correlation-U	-0.38	0.22	0.43	-0.23	0.01
Correlation-V	-0.39	0.42	0.30	0.21	0.01

#### 4.5 Evaluation of Monthly-mean Sea Surface Temperature

The default turbulence closure for the vertical eddy viscosity/diffusivity in FVCOM is the Mellor-Yamada level 2.5 turbulence model (MY-2.5). Han et al. (2011) reported that the heat flux could not penetrate deep enough when the MY-2.5 was used in an FVCOM simulation over the Grand Banks. As a result, the model mixed layer depth was too shallow in summer. Ma (2015) compared simulated SST based on  $k$ - $\epsilon$  closure and MY-2.5 closure with observations at three buoys, in which Buoy-c44251 is also enclosed in the model grid of this thesis (Fig 1-1), indicating that the model SST change from  $k$ - $\epsilon$  closure agrees well with observations, but those from the MY-2.5 closure do not. Thus, a second-order  $k$ - $\epsilon$  closure in GOTM is used here for our simulation.

Six-hourly simulated temperature at the first two sigma layers on the surface during Sep 1, 2010 and Aug 31, 2014 are interpolated onto Buoy-Mouth, Buoy-Red Island, Buoy-Head and Buoy-c44251 (See locations in Fig 3-1) each at the 0.5m depth and then averaged to get 48 monthly-mean SST to compare with the observational SST at 0.5m depth on each buoy location (Fig 4-3). It should be noted that several monthly-mean observations had NaNs at each Buoy because the percentage of the missing data in these months is higher than 40%. Besides, the monthly-mean values in Oct 2013 at Buoy-head are discarded because the position of the buoy changed during this month.

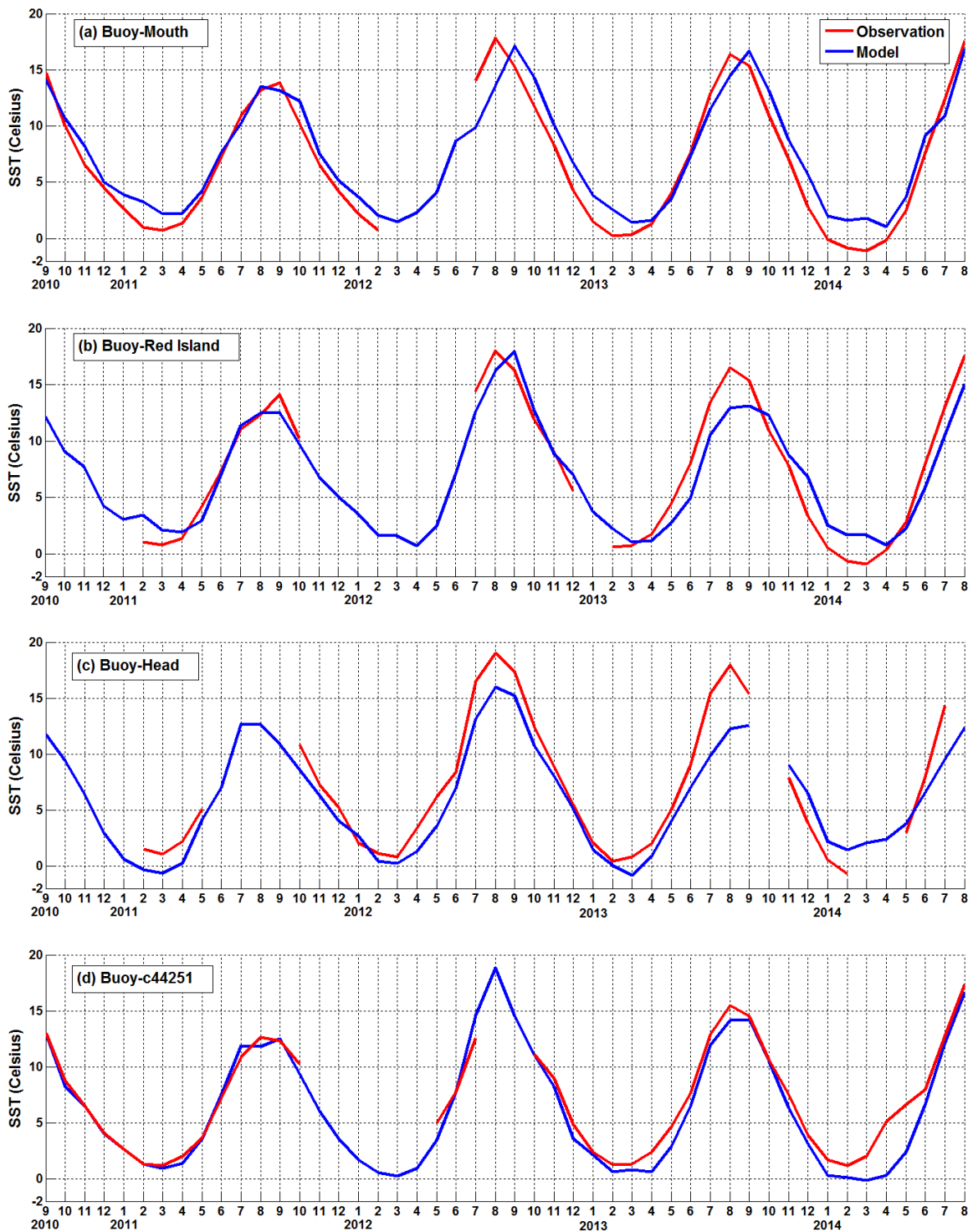


Fig. 4-3: Monthly-mean observed (red lines) and simulated (blue lines) SST at: (a) Buoy-Mouth, (b) Buoy-Red Islands, (c) Buoy-Head and (d) Buoy-c44251.

The simulated and observed SST at different buoys all had obvious similar seasonal

variabilities. The hottest SST usually happened in Aug/Sep with a relatively sharp peak, while the coldest SST usually occurred in Feb/Mar for the observation and from Jan to Apr for the models, both with a relatively flat trough.

At Buoy-Mouth (Fig 4-3a), the simulated SST reasonably reproduced the interannual variability of the observed ones. The simulated hottest/coolest Sep is in 2012/2011, and the simulated hottest/coolest Aug occurred in 2014/2011, which was consistent with the observations. The observation had the coldest Feb in 2014, while the simulated SST did not indicate obvious interannual differences. The largest difference between the simulated SST and the observed ones was about 4°C when the model underestimated the SST in Aug 2012. Besides, the model overestimated the SST in all winters.

At Buoy-Red Island, the simulated SST reasonably reproduced the interannual variability of the observed ones. The simulated hottest/coolest Aug and Sep occurred both in 2012/2011, which are consistent with the observations (except NaN observational SST in Sep 2010), but the simulation underestimated the SST in Aug 2013 and Sep 2013, with the largest difference (about 4°C) happened in Aug 2013; both the simulated SST and the observed ones had the coldest Feb in 2014, (except NaN observational SST in Feb 2012), however, the simulation all overestimated the SST in Feb.

At Buoy-Head, before Oct 2013 (when the buoy position changed), the simulated SST all underestimated the observed ones except Jan 2012, and the largest difference is about 6°C in Aug 2013. After Oct 2013-2014, the simulation agrees better. The simulated SST was hottest Sep in 2012 and coolest Sep in 2011, with a 5°C difference. Considering the poor observational quality and the movement of the buoy, it is difficult to compare the

simulation with the observation for the interannual time scales.

At Buoy-c44251, the simulated SST agrees well with the observed SST except during Mar and May 2014, when the model obviously underestimated SST, especially in Apr 2014 (with a 5°C difference). The simulated SST has coolest Aug in 2011 and the hottest Aug in 2014.

Quantitative comparisons are also made between the baseline simulation and observations using monthly-mean SST at Buoy-Mouth (Table 4-6), Buoy-Red Island (Table 4-7), Buoy-Head (Table 4-8) and Buoy-c44251 (Table 4-9). For the calculation of interannual statistics, if four or more NaN exist in any one-year period (starting from Sep), " - " will be applied instead of real statistics.

At Buoy-Mouth (Table 4-6), the RMSD, correlation coefficient and  $\gamma^2$  in the whole four-year duration (2010-2014, 48 months) are 1.66 °C, 0.97 and 0.07, demonstrating good agreement in terms of magnitude and variability. For the interannual comparison, 2010-2011 had the smallest RMSD (1.02°C), smallest  $\gamma^2$  (0.02), and highest correlation (0.99). The largest annual SST range is 16.2 °C in 2013-2014 for the baseline model and 18.7 °C in 2013-2014 for the observations.

At Buoy-Red Island (Table 4-7), the RMSD, correlation coefficient and  $\gamma^2$  in the whole four-year duration (2010-2014, 48 months) are 1.83 °C, 0.96 and 0.09, demonstrating good agreement in terms of magnitude and variability. The largest annual SST range is 17.8 °C in 2012-2013 for the model and 18.5 °C in 2013-2014 for the observations.

At Buoy-Head (Table 4-8), the RMSD, correlation coefficient and  $\gamma^2$  in the whole

four-year duration (2010-2014, 48 months) are 2.30 °C, 0.96 and 0.10, demonstrating good agreements in terms of variability but relatively large RMSD exists. The largest annual SST range is 18.2 °C in 2011-2012 for the baseline model and 18.2 °C in 2011-2012 for the observations.

At Buoy-c44251 (Table 4-9), the RMSD, correlation coefficient and  $\gamma^2$  in the whole four-year duration (2010-2014, 48 months) are 1.39 °C , 0.97 and 0.06, demonstrating good agreements in terms of magnitude and variability. For the interannual comparison, 2010-2011 had the smallest RMSD (0.46°C), smallest  $\gamma^2$  (0.01), and highest correlation (0.99). The largest annual SST range is 18.6 °C in 2011-2012 for the baseline model and 16.2 °C in 2013-2014 for the observations.

All of the correlation coefficients in Table 4-6, Table 4-7, Table 4-8 and Table 4-9, are significant in 95% confidence interval.

Table 4-6: Statistics from the comparison between observed and simulated monthly-mean SST at Buoy-Mouth

Buoy-Mouth: $k-\varepsilon$ .vs. Observation					
(Interannual Statistics)					
	2010-2011	2011-2012	2012-2013	2013-2014	Total
RMSD (°C)	1.02	-	1.64	1.80	1.66
Correlation	0.99	-	0.97	0.99	0.97
$\gamma^2$	0.02	-	0.06	0.03	0.07

Table 4-7: Statistics from the comparison between observed and simulated monthly-mean SST at Buoy-Red Islands

Buoy-Red Islands: $k-\varepsilon$ .vs. Observation					
(Interannual Statistics)					
	2010-2011	2011-2012	2012-2013	2013-2014	Total
RMSD (°C)	-	-	1.95	2.10	1.83
Correlation	-	-	0.94	0.96	0.96
$\gamma^2$	-	-	0.11	0.11	0.09

Table 4-8: Statistics from the comparison between observed and simulated monthly-mean SST at Buoy-Head

Buoy-Head: $k-\varepsilon$ .vs. Observation					
(Interannual Statistics)					
	2010-2011	2011-2012	2012-2013	2013-2014	Total
RMSD (°C)	-	1.96	2.62	-	2.30
Correlation	-	0.99	0.97	-	0.96
$\gamma^2$	-	0.04	0.08	-	0.10

Table 4-9: Statistics from the comparison between observed and simulated monthly-mean SST at Buoy- c44251

Buoy-c44251: $k-\varepsilon$ .vs. Observation					
(Interannual Statistics)					
	2010-2011	2011-2012	2012-2013	2013-2014	Total
RMSD (°C)	0.46	-	1.09	2.13	1.39
Correlation	0.99	-	0.99	0.97	0.97
$\gamma^2$	0.01	-	0.01	0.08	0.06

## **5. Interannual Variability of Monthly-mean Circulation, SST and Stratification**

As shown in previous studies (Han, 2005; Han et al., 2008; Ma, 2010; Ma 2015), the circulation, SST and stratification around Placentia Bay at different time scales were influenced by various factors, such as topography; local net heat flux and wind; remote water inflow from the inshore branch of Labrador Current. In this chapter, the roles of these various factors which may affect the interannual variability of monthly-mean circulation, SST pattern and stratification will be identified.

### **5.1 Transports at different Transects**

The simulated transports along three different transects (Fig 5-1) are plotted in Fig 5-2 and Fig 5-3. The 53.5°W Transect is set across Avalon Channel between the outer 100m contour line and onshore coast to calculate transports associated with the inshore branch of Labrador Current; the 46.9°N Transect is set across eastern outer bay where the depth is shallower than 200m to calculate the transports flow into the outer bay; the 47.5°N Transect is set across eastern inner bay to calculate the transports flow into the inner bay. Positive transport is westward or northward. Table 5-1 shows the related annual statistics of the transports through these three transects.

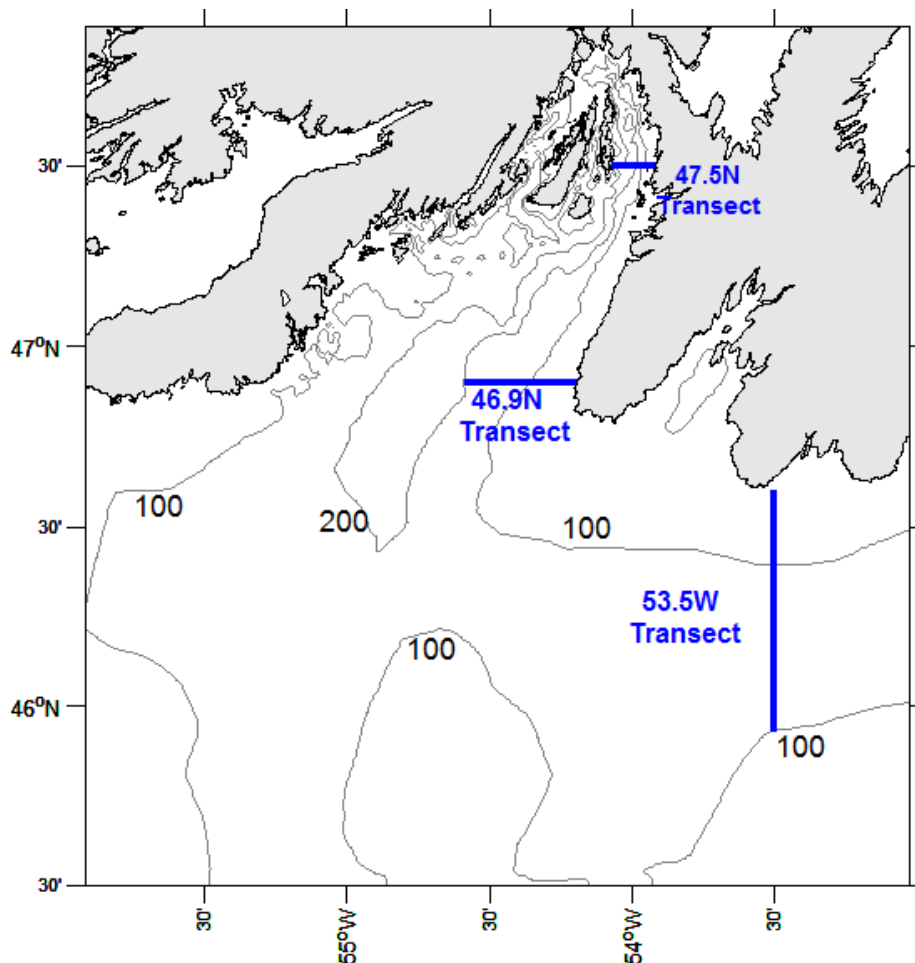


Fig. 5-1: Map showing the three transects used to calculate water transport there. The isobaths displayed are 100 and 200m contour lines.

The model monthly-mean transports at the 53.5W Transect associated with the inshore branch of Labrador Current through Avalon Channel and onshore coast (Fig 5-2, Fig 5-3a) showed distinct seasonal and interannual variability. The largest interannual variability happened in Nov with a standard deviation of 0.37 Sv, and the range between Nov 2010 and Nov 2013 reached 0.78 Sv; the smallest interannual variability occurred in Apr with a standard deviation of 0.05 Sv, and the range between Apr 2013 and Apr 2014 was only 0.12 Sv. According to Table 5-1, the annual mean transports in 2011, 2012 and

2013 were 0.70 Sv, 0.75 Sv and 0.97 Sv (positive westward).

The simulated transports at 46.9N Transect (Fig 5-2, Fig 5-3b) showed similar seasonal and interannual variability with those at 53.5W Transect. The largest interannual variability happened in Dec with a standard deviation of 0.27 Sv, and the range between Nov 2010 and Nov 2013 reached 0.57 Sv; the smallest interannual variability occurred in Apr with a standard deviation of 0.02 Sv, and the range between Apr 2013 and Apr 2014 was only 0.05 Sv. The correlation between transports at 46.9N Transect and transports at 53.5W Transect is 0.93, indicating that the transports flowed into the bay were dominated by the westward transports through Avalon Channel and its onshore coast originated from the inshore branch of Labrador Current. The annual mean transports in 2011, 2012 and 2013 were 0.56 Sv, 0.58 Sv and 0.69 Sv (westward), which is positively correlated to the interannual variability of the transports through the 53.5°W Transect. The model results suggested that 80%, 77% and 72% of the inshore branch of Labrador Current entered Placentia Bay through eastern outer bay in 2011, 2012 and 2013.

The model transports at 47.5N Transect (Fig 5-3c) were all too weak to have obvious seasonal or interannual variability, and 80% of the monthly-mean transports were in northward direction. The correlation between transports at 53.5°W Transect and transports at 47.5N Transect is 0.19, indicating that the transports of the inner bay area were less correlated to the transports originated from the eastern outer bay.

Table 5-1: Annual statistics of the transports through 53.5°W, 46.9°N and 47.5°N Transect

Transport (Sv)			
	2011	2012	2013
53.5°W Transect	0.70	0.75	0.97
46.9°N Transect	0.56 (80%)	0.58 (77%)	0.69 (72%)
47.5°N Transect	0.004	0.005	0.006

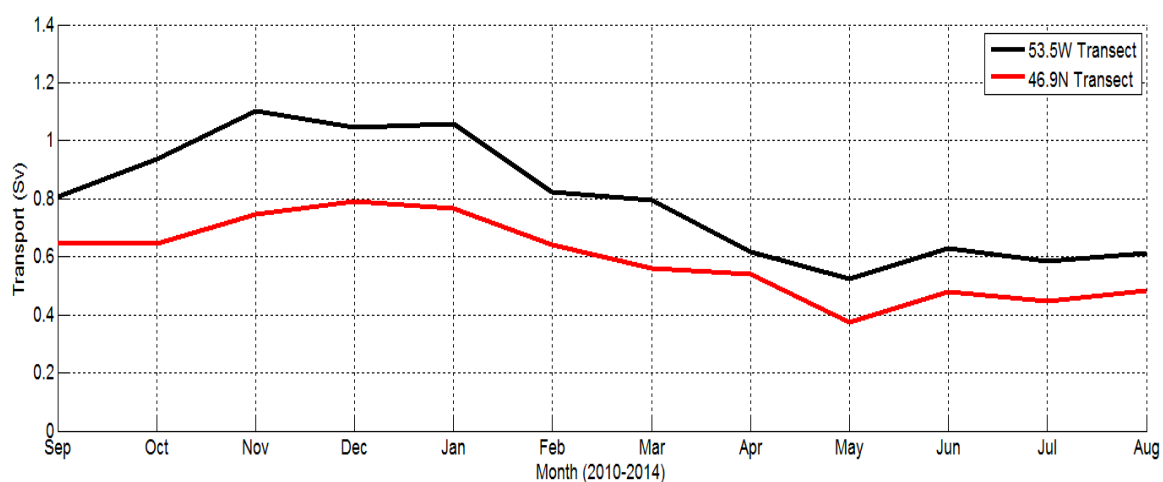


Fig. 5-2: Seasonal-mean transport on 53.5W Transect (black line) and 46.9N Transect (red line).

Positive transport is westward or northward.

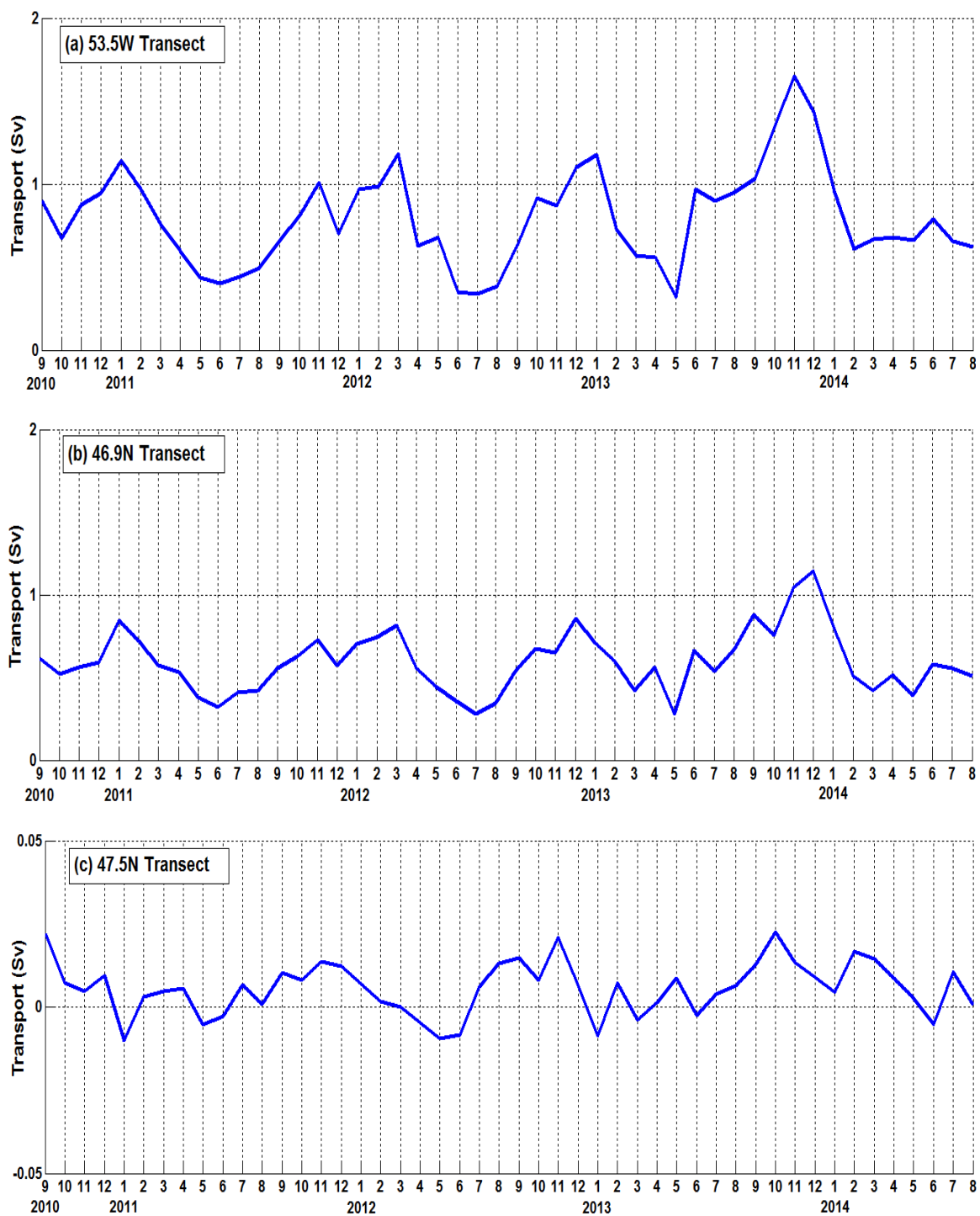


Fig. 5-3: Monthly-mean simulated transport (Sv) at three different transects: (a) 53.5°W Transect; (b) 46.9°N Transect and (c) 47.5°N Transect. Positive transport is westward or northward.

## 5.2 Circulation

To identify the roles of local wind and remote water inflow from the inshore branch of Labrador Current on the interannual variability of monthly-mean current over Placentia Bay, surface circulation, depth-averaged (0-30m) circulation and horizontal sea level distributions of Dec 2011, Dec 2012 and Oct 2010 are plotted here (Fig. 5-4, Fig. 5-5 and Fig. 5-6). According to the model validation results presented in chapter 4 (Fig. 4-1 and Fig. 4-2), the simulated sea level anomalies and surface currents at these three months showed good agreement with the observations (except the surface currents comparisons for the inner bay area).

### 5.2.1 Interannual Variability Dec 2011 and Dec 2012

There were relatively large differences of sea level anomalies and surface currents at Buoy-Mouth between Dec 2011 and Dec 2012 (Fig. 4-1 and Fig. 4-2a/b), showing obvious interannual variabilities.

In Fig. 5-4, under a spatially-averaged monthly-mean northeastward wind ( $2.4 \text{ m/s}$ ), the difference between surface circulation and depth-averaged (0-30 m) circulation of Dec 2011 was small over the whole domain; in Fig. 5-5, under a spatially-averaged monthly-mean southeastward wind ( $2.3 \text{ m/s}$ ), the difference between surface circulation and depth-averaged (0-30m) circulation of Dec 2012 was also small over the whole domain. The two comparisons indicated that it is difficult for the relatively small monthly-mean wind to influence the surface circulation. The surface circulation is consistent with the depth-averaged (0-30m) circulation, which was mainly affected by remote water inflow from

the inshore branch of Labrador Current.

In Fig. 5-4 and Fig. 5-5, the circulation in the upper ocean (0-30 m) of Dec 2011 and Dec 2012 was dominated by a similar cyclonic gyre in the outer area of Placentia Bay, consistent with the general circulation pattern from previous studies, but with different intensities. Currents of the gyre on Dec 2011 had smaller amplitudes (up to around 0.2 *m/s*), headed southward after flowing out of the bay from the western coast, and then out of the domain from southern open boundary between St. Pierre Bank and Green Bank; Meanwhile, currents of the gyre on Dec 2012 had larger amplitudes (up to around 0.3 *m/s*), which was possible to partially flow westward and then out of the domain from western open boundary. In the middle part of bay, the weaker cyclonic gyre on Dec 2011 can flow further to 47°20'N until reaching Red Island, while the stronger cyclonic gyre on Dec 2012 can only reach 47°12'N. For the inner bay area where the cyclonic gyre cannot reach, the currents there were both very weak, except an obvious northward current (up to 0.15 *m/s*) along the eastern inner bay which was influenced by part of the northward inflow from the eastern outer bay in Dec 2011.

According to the horizontal sea level distributions in Fig. 5-4 and Fig. 5-5, the cyclonic gyre corresponded well to the sea level slope (higher nearshore) oriented from eastern open boundary. Under geostrophic assumption, the sea level slope of Dec 2012 at Avalon Channel and onshore coast near eastern open boundary is steeper than that of Dec 2011, indicating larger westward transports there based on the inshore branch of Labrador Current, which is consistent with the monthly-mean model transports at 53.5W Transect in Fig 5-3a (The transport was 0.7 Sv on Dec 2011 and 1.1Sv on Dec 2012). The gentler

but wider sea level slope on Dec 2011 in the middle part of the bay explained the further but weaker gyre on Dec 2011, compared to that on Dec 2012. When the currents steered out of the bay from the western coast, the sea level slopes there on Dec 2011 were mainly in western-eastern direction (higher on the west), resulting in southward outflow; the sea level slopes there on Dec 2012 were separated into both western-eastern direction (higher on the west) and northern-southern direction (higher on the north), creating both westward and southward outflow. The sea level slope over the inner bay area on both Dec 2011 and Dec 2012 were very weak and hardly influenced by the remote sea level slope from the outer bay, consistent with the monthly-mean model transports at 47.5N Transect in Fig 5-3c (The transport were both nearly 0 Sv on Dec 2011 and on Dec 2012).

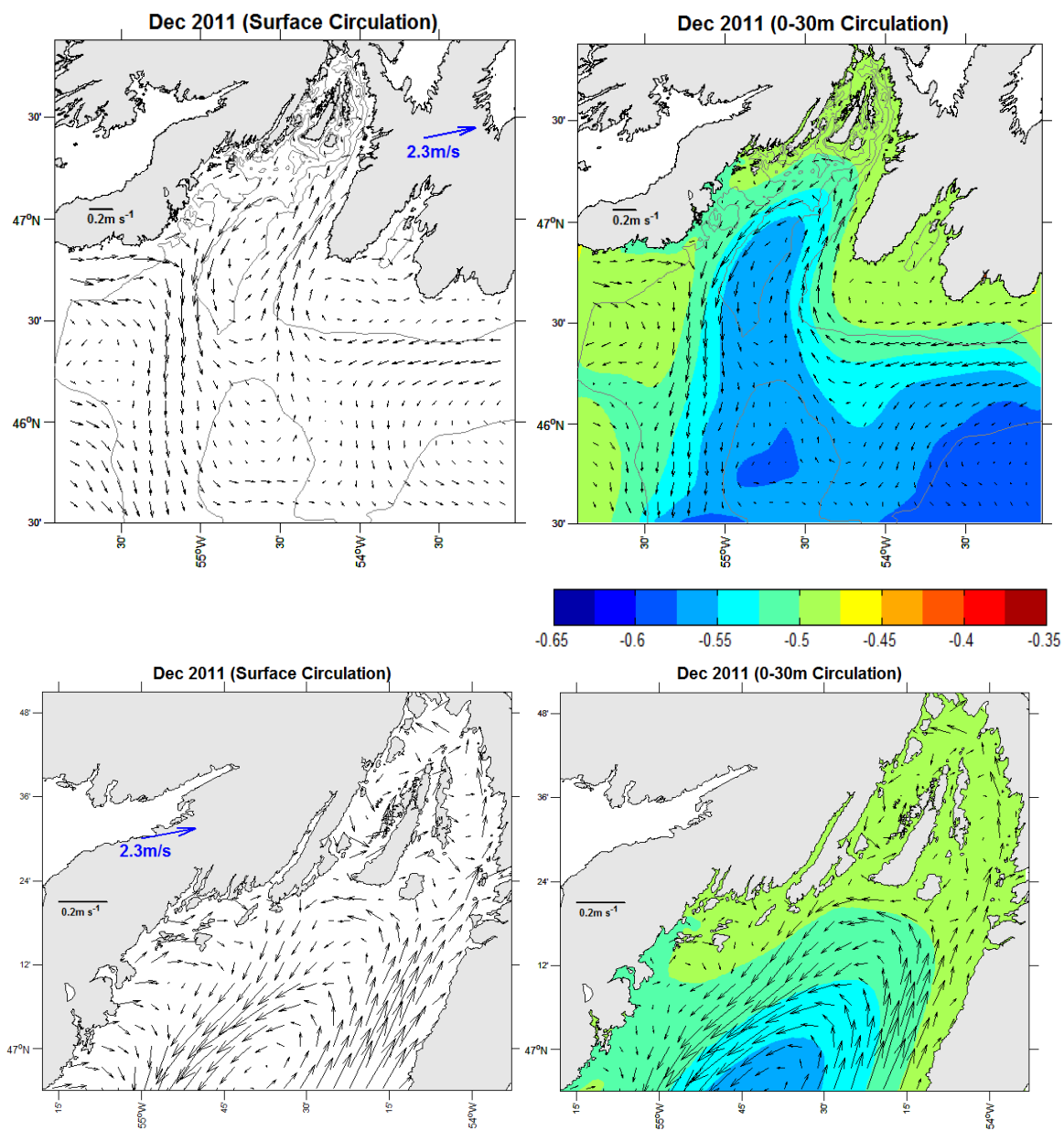


Fig. 5-4: Monthly-mean simulated surface/depth-averaged (0-30 m) circulation, horizontal sea level distributions and the corresponding close-ups for the inner bay area of Dec 2011. The spatially-averaged monthly-mean NARR wind vector at 10m high above the ocean is shown in the surface circulation map.

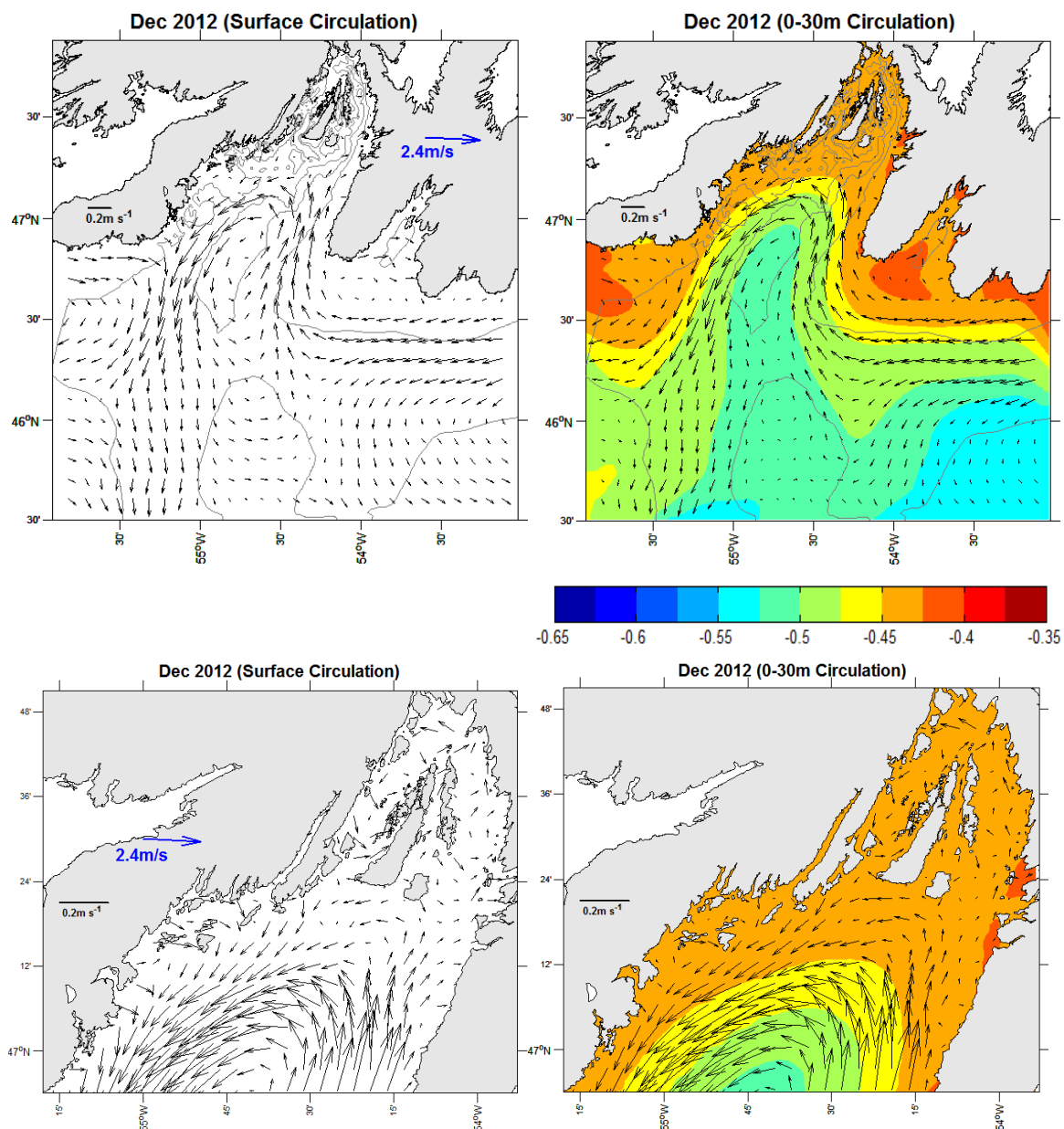


Fig. 5-5: Monthly-mean simulated surface/depth-averaged (0-30 m) circulation, horizontal sea level distributions and the corresponding close-ups for the inner bay area of Dec 2012. The spatially-averaged monthly-mean NARR wind vector at 10 m high above the ocean is shown in the surface circulation map.

### 5.2.2 Local Wind Effect on Surface Circulation

In Fig. 5-6, the amplitude of the spatially-averaged monthly-mean NARR wind on Oct 2010 (4.6  $m/s$ ) was twice as large as those on Dec 2011 and Dec 2012, which made distinct surface circulation patterns compared to depth-averaged (0-30 m) circulation. The surface currents of Oct 2010 was influenced mainly by the relatively strong northeastward wind, advecting eastward surface currents from west open boundary, and the general cyclonic gyre due to the inshore branch of Labrador Current was not clearly defined. Part of eastward surface currents followed the 200 m contour line outside the bay and steered northeastward into the bay on its eastern side (up to 0.2  $m/s$ ), and then flowed northeastward along the eastern coast into the middle part of the bay (reduced to 0.1  $m/s$ ); the currents over the inner bay area were dominated by eastward wind-driven components; in Avalon Channel and its onshore coast, the eastward wind-driven components were mostly offset by remote surface inflow from the east open boundary.

The depth-averaged (0-30 m) circulation on Oct 2010 was still dominated by the general cyclonic gyre in the outer bay area, with its intensity and pattern very similar to those on Dec 2011 (Fig. 5-4). This is because the monthly-mean model transports at 53.5W and 46.9N Transect (Fig 5-3a, Fig 5-3b) and on Oct 2010 and Dec 2011 were nearly the same.

Overall, the monthly-mean surface circulation could only be affected by relatively large monthly-mean local wind. However, during the entire simulation period (totally 48 months), there were only six months which owned relatively strong wind with the spatially-averaged amplitude larger than 4.0 $m/s$ , indicating that the simulated monthly-

mean upper ocean circulation in Placentia Bay was primarily mostly influenced by remote water inflow from the inshore branch of Labrador Current.

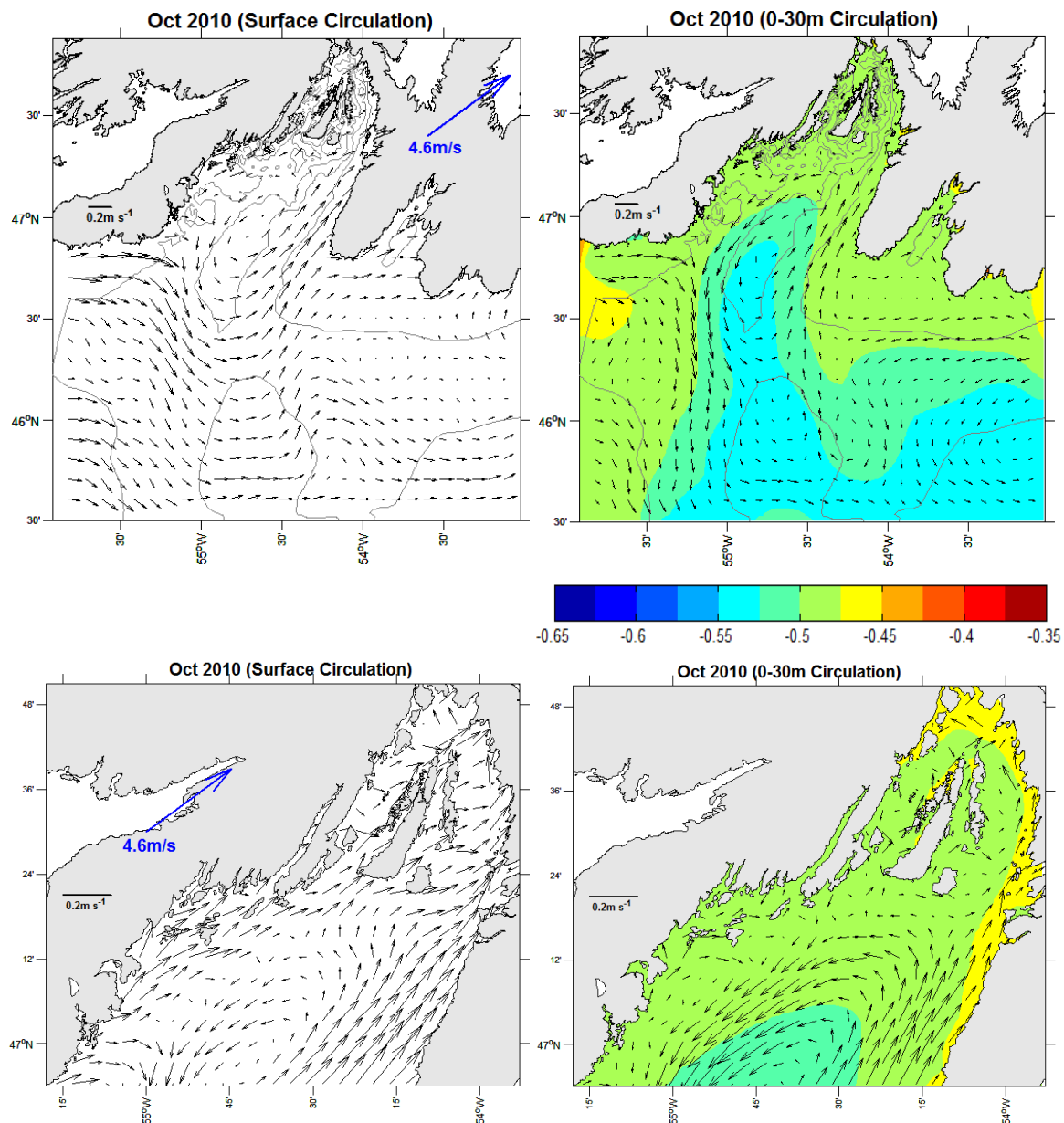


Fig. 5-6: Monthly-mean simulated surface/depth-averaged (0-30m) circulation, horizontal sea level distributions and the corresponding close-ups for the inner bay area of Oct 2010. The spatially-averaged monthly-mean NARR wind vector at 10m high above the ocean is shown in the surface circulation map.

### 5.3 Sea Surface Temperature

To analyze the factors which affect the interannual variability of monthly-mean surface temperature over Placentia Bay, the monthly-mean surface temperature distributions on Aug 2010 and Aug 2014 are plotted here (Fig. 5-7). According to the model validation results in chapter 4 (Fig. 4-3), the simulated monthly-mean time-series SST at these two months both had good agreement with the observed monthly-mean time-series SST, except that there were no observed SST at Bouy-Head. The simulated SST, observed air temperature and interpolated NARR net heat flux on both Aug 2011 and Aug 2014 at four buoys were listed in Table 5-1. (see Fig. 2-4, Fig 3-3 and Fig. 4-3 for the corresponding values).

As shown in Table 5-1, the simulated SST on Aug 2011 at Buoy-c44251, Bouy-Mouth, Buoy-Red Island and Buoy-Head were about 11.8°C, 13.9°C, 13.6°C, and 13.4°C, while the simulated SST on Aug 2014 at these four buoys were 16.7°C, 17.1°C, 15.8°C and 13.0°C, indicating obvious interannual and spatial variations. The SST on Aug 2011 was lower than the SST on Aug 2014 except those at Bouy-Head which were nearly the same; the amplitude differences of the simulated SST between the two months decreased from the outer bay to the inner bay (4.9°C, 3.2°C, 2.2°C and -0.4°C). The close positive correlations among the simulated SST, the observed air temperature and NARR net heat flux can be seen. The larger NARR net heat flux over the whole domain ( $200 W/m^2$ ) on Aug 2014 may lead to higher SST than the smaller net heat flux ( $160 W/m^2$ ).

The monthly-mean surface temperature distributions in Placentia Bay (Fig. 5-7) showed interannual differences on Aug 2011 and Aug 2014, which agreed with the

comparison in Table 5-2. Besides, the interannual temperature variability of the water inflow advected from the eastern open boundary seems also important for the outer bay temperature pattern. However, the model seems to overestimate the southeastward cold water fronts formed across the western coast on both Aug 2011 and Aug 2014, because the amplitude of the spatially-averaged monthly-mean NARR winds on Aug 2011 ( $0.8m/s$ ) and Aug 2014 ( $0.8m/s$ ) were both too weak to make any substantial contribution.

Table 5-2: Statistics of the simulated SST, observed air temperature and interpolated NARR net heat flux on both Aug 2011 and Aug 2014 at four buoys

	Simulated SST (°C)		Observed Air Temp (°C)		NARR Net Heat Flux ( $W/m^2$ )	
	Aug 2011	Aug 2014	Aug 2011	Aug 2014	Aug 2011	Aug 2014
Buoy-c44251	11.8	16.7	NaN	NaN	160	200
Buoy-Mouth	13.8	17.1	13.1	17.3	160	200
Buoy-Red Island	13.6	15.8	13	16.6	160	200
Buoy-Head	13.4	13.0	NaN	17.1	160	200

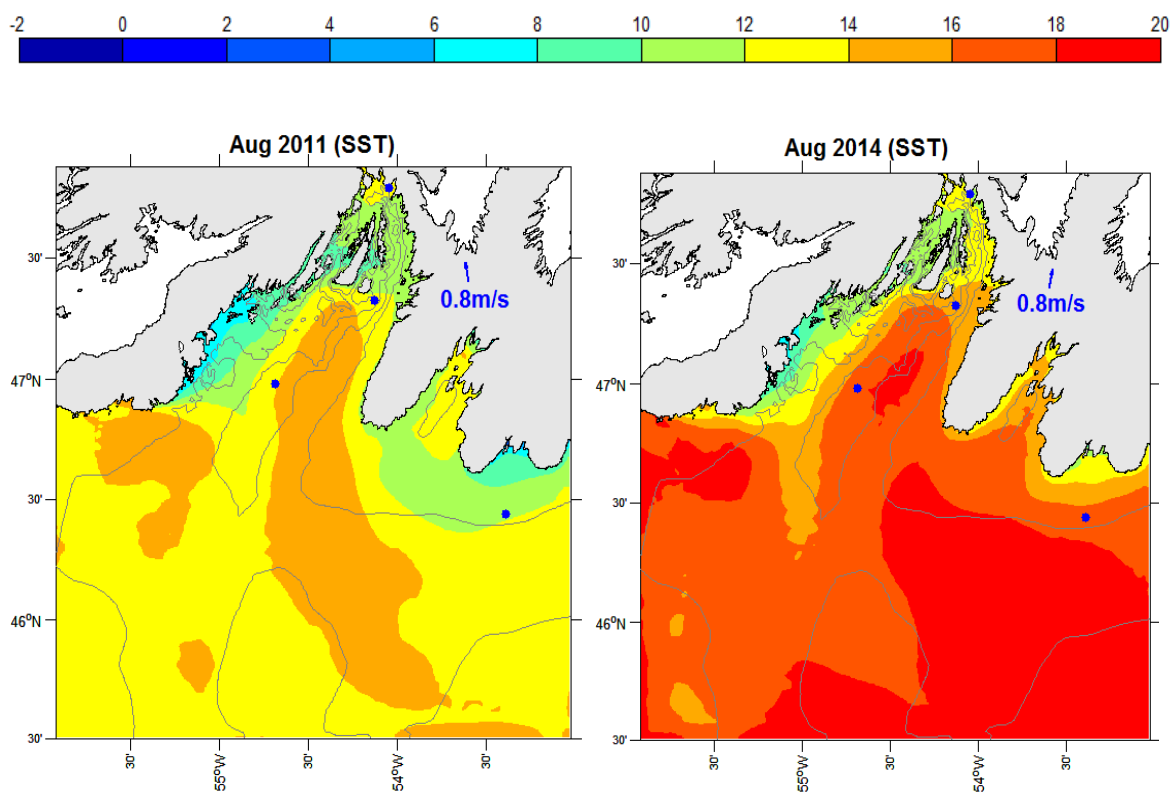


Fig. 5-7: Monthly-mean simulated SST of Aug 2011 and Aug 2014. The spatially-averaged monthly-mean NARR wind vectors at 10m high above the ocean are shown. The blue dots from the outer to inner bay represent location of Bouy-Mouth, Buoy-Red Island, Buoy-Head and Buoy-c44251.

## 5.4 Stratification and Mixed Layer Depth

The development of stratification can be affected by local wind (Ma et al., 2015) and net heat flux at the sea surface (Ma et al., 2012). The wind-driven turbulence could interrupt strong stratification and deepen the mixed layer. When the net heat flux increases, the mixed layer depth shallows as the stratification increases. In this thesis, the 4-year long-term model simulations provide a detailed representation of the interannual and spatial variability of monthly-mean stratification and mixed-layer depth around Placentia Bay during Sep 2010 and Aug 2014.

### 5.4.1 Monthly-mean Depth-averaged (0-50m) Buoyancy Frequency ( $N^2$ ) and Richardson Number (Ri)

In oceanography, the buoyancy frequency ( $N^2$ ) represents stability of the vertical density distribution by  $N^2 = -\frac{g}{\rho_0} \frac{d\rho}{dz}$  and can be negative or positive. A larger positive  $N^2$  represents an intensified vertical stratification and need stronger vertical current shear to disrupt, while a negative  $N^2$  corresponds to a fluid with the greater densities above lesser densities, which leads to unstable status; the Richardson Number (Ri) expresses the ratio of buoyancy term and flow shear term by equation  $Ri = \frac{N^2}{M^2}$ , where  $M = \left| \frac{d\bar{u}}{dz} \right|$  is called the Prandtl frequency representing horizontal current shear.

To assess and compare the strength of stratification around Placentia Bay quantitatively, monthly-mean depth-averaged (0-50 m) buoyancy frequency ( $N^2$ ) and Richardson number (Ri) at Buoy-Mouth and Buoy-Red Island are shown in Fig. 5-8 and

Fig. 5-9. Two critical Richardson Number ( $Ri=0.25$ ;  $Ri=1$ ) mentioned in Chapter 2.3.2 are also plotted in Fig 5-9 to evaluate the stability of the stratified shear flow in the upper ocean around Placentia Bay.

The buoyancy frequency  $N^2$  (in Fig. 5-8) is usually strongest in summer and weakest in winter with a positive correlation to the evolution of surface net heat flux. Besides, interannual variability of can be seen in Fig. 5-8. The  $N^2$  during summer (from Jun to Aug) 2013 at both Buoy-Mouth and Buoy-Red Island were smaller than the other three summers, indicating a weaker stratification at 0-50m depth during summer 2013; The  $N^2$  during summer 2012 at Buoy-Mouth and summer 2014 at Buoy-Red Island were each larger than the other three summers at the same site.

The stability ( $Ri$ ) of the stratified shear flow in the upper ocean (0-50m) around Placentia Bay was determined by the strength of stratification  $N^2$  and horizontal current shear  $M^2$  (Fig. 5-9). At Buoy-Mouth,  $Ri$  during late 2010 and early 2011 (Nov 2010~Apr 2011) was U-shaped and close to 0.25, nearly unstable in late fall and winter, while  $Ri$  on the other three years at the same season (Nov 2011~Apr 2012, Nov 2012~Apr 2013 and Nov 2013~Apr 2014) were V-shaped and the stratification only in middle winter were nearly unstable. Among all the four periods, the Nov 2011~Apr 2012 period was least unstable. The  $Ri$  at Buoy-Red Island were overall larger than that at Buoy-Mouth, but had similar interannual variability.

The monthly-mean observed air temperature at Buoy-Mouth and Buoy-Red Island mentioned in Fig. 3-3 (blue line and red line) was also analyzed to investigate its relation to the interannual evolution of stratification. The winter of 2012 had slightly warmer air

temperature than the other three winters, which may contribute to the more stable stratification in the upper ocean (0-50 m) at Buoy-Mouth in the winter of 2012 (see Fig. 5-9).

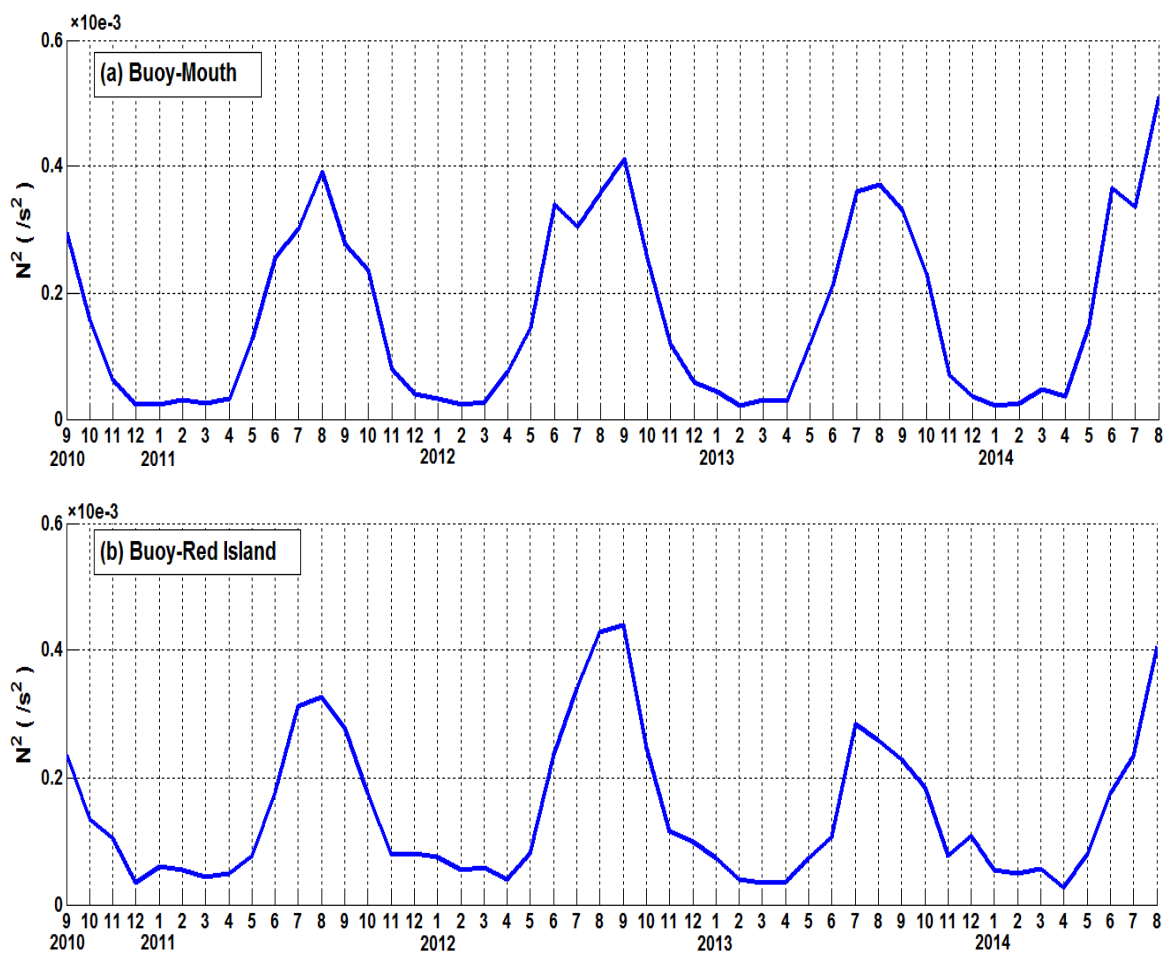


Fig. 5-8: Monthly-mean depth-averaged (0-50m) buoyancy frequency ( $N^2$ ) at: (a) Buoy-Mouth and (b) Buoy-Red Island.

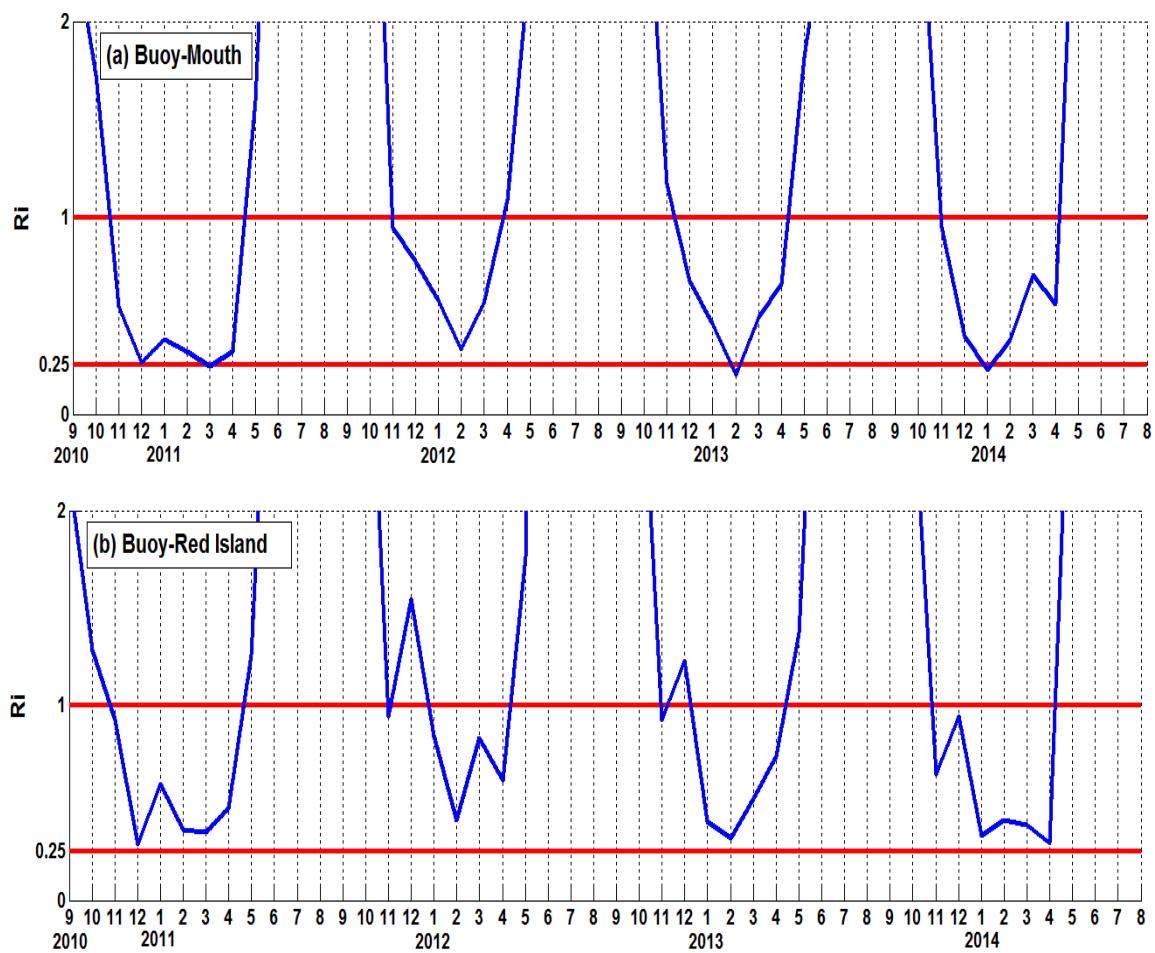


Fig. 5-9: Monthly-mean depth-averaged (0-50m) Richardson Number (Ri) at: (a) Buoy-Mouth, (b) Buoy-Red Island. The red lines are critical Richardson Number.

### 5.4.2 Monthly-mean Mixed Layer Depth

To further elucidate the above phenomenon, monthly-mean mixed layer depth (MLD) at Buoy-Mouth and Buoy-Red Island are also examined (Fig 5-10) according to the sigma- $t$  (density) criterion used in Levitus (1982) which uses the depth at which a density change from the ocean surface sigma- $t$  of  $0.125 \text{ kg/m}^3$  has occurred.

At Buoy-Mouth, the mixed layer depth on Feb 2014 was 50  $m$ , about 10  $m$  deeper than the other three Feb, which is positively correlated to the interannual variations of the observed air temperature at Buoy-Mouth (Fig. 3-3), when the air temperature on Feb 2014 was coldest at  $-4^\circ\text{C}$ ; the mixed layer depth on Mar 2014 was 27  $m$ , about 10  $m$  shallower than the other three Mar, which is positively correlated to the interannual variations of the NARR net heat flux at Buoy-Mouth location (Fig. 2-4), when the net heat flux on Mar 2014 was highest at  $180 \text{ W/m}^2$ .

At Buoy-Red Island, the mixed layer depth on Dec 2010 was about 38  $m$ , which is about 20  $m$  deeper than the other three Dec. This is probably due to large turbulences created by the relatively strong monthly-mean southwestward winds on Dec 2010 (Fig. 2-3). From Nov 2010 to Dec 2010, the wind direction change was much more distinct compared with those from Nov 2011 to Dec 2011, from Nov 2012 to Dec 2012 and from Nov 2013 to Dec 2013.

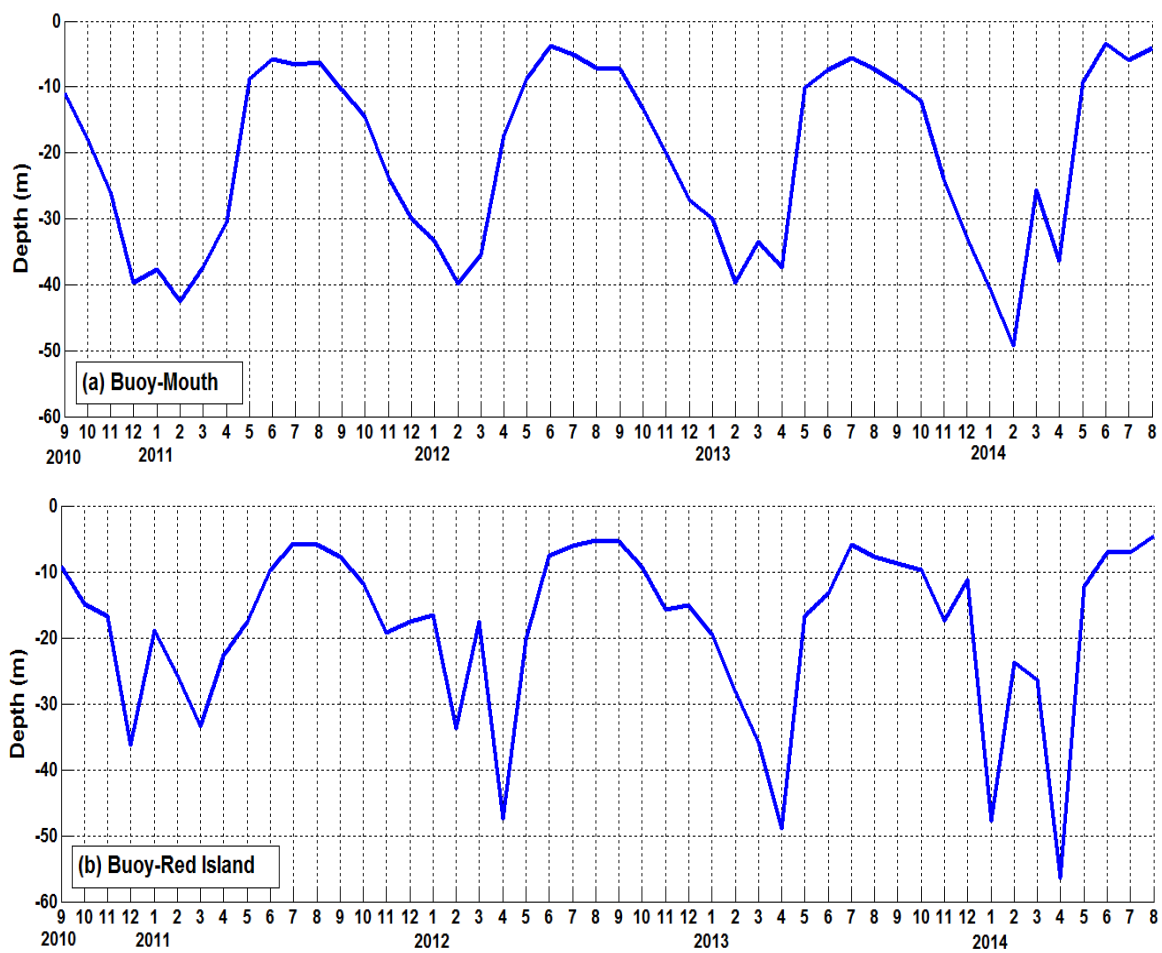


Fig. 5-10: Monthly-mean Mixed Layer Depth at: (a) Buoy-Mouth and (b) Buoy-Red Island.

## 6. Summary

In this thesis, an application of a long-term (four consecutive years), three-dimensional, full-prognostic and baroclinic model based on FVCOM is developed to simulate the interannual variability of circulation, sea surface temperature and stratification around Placentia Bay.

Initialized from a still state with a climatological monthly-mean temperature and salinity fields, the model is forced by spatial and temporal changed winds and heat fluxes from NARR dataset on the surface; five leading tidal constituents specified on the open boundary from a large-scale Newfoundland Shelf model; non-tidal sea level, temperature and salinity on the open boundary from HYCOM output; an additional empirical constant sea level slope on the selected east open boundary to adjust the transports from the inshore branch of Labrador Current, and same sea level slope (opposite sign) on the selected west open boundary to ensure the conservation of the kinetic energy. The model results have been compared and evaluated against observations at tide-gauge stations and mooring buoys. Overall, the model simulates monthly mean water levels, surface currents and SST well.

The averaged RMSD, correlation coefficients and  $\gamma^2$  between the observed and simulated monthly-mean sea level anomalies at two tide gauge stations are 4 cm, 0.74 and 0.77 for the whole four years, with the smallest RMSD happened in 2011-2012 (2.1 cm averaged).

The RMSD, SDR and VDR values between the observed and simulated monthly-mean surface current U/V in the whole four-year duration are 0.06/0.05 m/s, and 0.29 and 0.42 at Buoy-Mouth, capturing magnitude and direction well; 0.05/0.11 m/s, 0.36 and

1.62 at Buoy-Red Island, indicating fairly good agreement with observation. The SDR and VDR values at Buoy-Head are too large, showing poorly ability to reproduce real surface currents there.

The RMSD, correlation coefficient and  $\gamma^2$  between the observed and simulated monthly-mean SST in the whole four-year duration are 1.66 °C, 0.97 and 0.07 at Buoy-Mouth; 1.83°C, 0.96 and 0.09 at Buoy-Red Island; 2.30 °C, 0.96 and 0.09 at Buoy-Head; 1.39 °C, 0.97 and 0.06 at Buoy-c44251. All the statistics indicate good agreement in terms of magnitude and variability.

The horizontal surface and depth-averaged (0-30 m) circulation on Dec 2011 and Dec 2012 showed obvious interannual variations. In the outer bay area, the general monthly-mean circulation pattern in the upper ocean was cyclonic into the bay on the eastern side and out on the western side, but with different intensities depended on the intensities of the remote westward water inflow from the inshore branch of Labrador Current, resulting in larger current amplitudes of the cyclonic gyre on Dec 2012 compared to those on Dec 2011. The horizontal sea level distributions showed that the cyclonic gyre corresponded well to the sea level slope (higher nearshore) oriented from eastern open boundary under geostrophic assumption. Over the inner bay area, currents in the upper ocean were much weaker due to the reduced affection from the cyclonic gyre. The surface circulation patterns on both Dec 2011 and Dec 2012 were very similar to their related depth-averaged (0-30 m) circulation patterns, indicating that the relatively small monthly-mean local wind forcing was difficult to influence the surface circulation. However, when the amplitude of the monthly-mean local wind forcing was relatively

strong at several months such as Oct 2010 (minority during model period), the wind effect could be as important as influence from the remote water inflow on the surface circulation.

The monthly-mean surface temperature distributions on Aug 2010 and Aug 2014 showed distinct interannual variations positively correlated to the observed air temperature, the net heat flux on the sea surface and the water inflow advected from the inshore branch of the Labrador Current. However, the model seems to overestimate the southeastward cold water fronts formed across the western coast on both Aug 2011 and Aug 2014.

The depth-averaged (0-50 m) buoyancy frequency ( $N^2$ ), Richardson Number (Ri) and the mixed layer depth at Buoy-Mouth and Buoy-Red Island also showed interannual variabilities which may be positively correlated to the interannual variations of some other variables, such as wind intensity, air temperature, and net heat flux.

## Reference:

- Abarbanel, H. D., D. D. Holm, J. E. Marsden, and T. Ratiu, 1984: Richardson number criterion for the non-linear stability of 3D stratified flow. *Phys. Rev. Lett.*, 52, 2352–2355.
- Bradbury, I.R.; Snelgrove, P.V.R., Fraser, S., 2000. Transport and development of eggs and larvae of Atlantic cod, *Gadus morhua*, in relation to spawning time and location in coastal Newfoundland. *Can. J. Fish. Aquat. Sci.* 57: 1761–1772.
- Bradbury, T.R., B.J. Laurel., D. Robichaud, G.A. Rose. P.V.R. Snelgrove, R.S. Gregory, D. Cote, M.J.S. Wmdle, 2008, Discrete spatial dynamics in a marine broadcast spawner. Re-evaluating scales of connectivity and habitat associations in Atlantic cod (*Gadus morhua* L.) in coastal Newfoundland, *Fisheries research*, 91, 299-309.
- Burchard, H. 2001. Simulating the wave-enhanced layer under breaking surface waves with two-equation turbulence models. *J. Phys. Oceanogr.*, 31, 3133-3145.
- Canuto, V. M., A. Howard, Y. Cheng and M. S. Dubovikov, 2001. Ocean turbulence. Part I: one point closure model-momentum and heat vertical diffusivities. *J. Phys. Oceanogr.*, 31, 1413-1246.
- Catto, N.R., Anderson, M.R., Scruton, D.A. and Williams, U.P., 1997. Coastal Classification of The Placentia Bay Shore. Canadian Technical Report of Fisheries and Aquatic Sciences No. 2186
- Chen, C., H. Liu and R.C. Beardsley (2003), An unstructured grid, finite volume primitive equation coastal ocean model: application to coastal ocean and estuaries. *J. Atmos. Ocean. Technol.*, 20, 159–186.
- Chen C, G. Cowles and R.C. Beardsley, 2013. An unstructured grid, Finite-Volume Community Ocean Model: FVCOM User Manual, 4th Edition. SMAST/UMASSD Technical Report-130701.
- Courant, R., K.P. Friedrichs, and H. Lewy, 1928: 'Über die partiellen Differenzgleichungen der mathematischen Physik. *Math. Annalen*, 100, 32–74.
- Cowles, G. W., S. J. Lentz, C. Chen, Q. Xu, and R. C. Beardsley (2008), Comparison of observed and model-computed low frequency circulation and hydrography on the New England Shelf, *J. Geophys. Res.*, 113, C09015, doi:10.1029/2007JC004394.
- Cushman-Roisin and Beckers. 2011. Introduction to Geophysical Fluid Dynamics, 2nd edition. AP, International Geophysics Series, Volume 101.
- deYoung, B., Otterson, T., Greatbatch, R.J., 1993. The local and nonlocal response of Conception Bay to wind forcing. *J. Phys. Oceanogr.* 23, 2636-2649.

- Galperin, B., L.H.Kantha, S.Hassid, and A.Rosati, 1988. A quasi-equilibrium turbulent energy model for geophysical flows, *J.Atoms.Sci.*,45,55-62.
- Galperin, B., S. Sukoriansky and P. Anderson. 2007. On the critical Richardson number in a stably stratified turbulence. *Atmos. Sci. Lett.* 8(3), 65-69.
- Geshelin, y., J.Sheng, and R.J.Greatbatch, 1999. Monthly mean climatologies of temperature and salinity in the western North Atlantic, Can. Tech. Rep. Hydrogr. Ocean Sci. 153,62 pp., Ocean Sci. Div. of Fish. and Ocean Can., Dartmouth, N. S., Canada.
- Greenberg, D.A, and B.D.Petrie, 1988. The mean barotropic circulation on the Newfoundland shelf and slope, *Journal of geophysical research*, 93, 15541-15550.
- Han, G. 2000. Three-dimensional modelling of tidal currents and mixing quantities over the Newfoundland Shelf. *J. Geophys. Res.* 105, 11407-11422.
- Han, G. 2005. Wind-driven barotropic circulation off Newfoundland and Labrador. *Cont. Shelf Res.* 25, 2084-2106.
- Han, G., Lu, Z., Wang, Z., Helbig, J., Chen, N., deYoung, B., 2008. Seasonal variability of the Labrador Current and shelf circulation off Newfoundland. *J. Geophys. Res.* 113, 1-23.
- Han, G., Paturi, S., de Young, B., Yi, S., Shum, C.-K., 2010. A 3-D data-assimilative tide model of Northwest Atlantic. *Atmosphere-Ocean.* 48, 39-57
- Han, G., Ma, Z., de Young, B., Foreman, M., Chen, N., 2011. Simulation of three-dimensional circulation and hydrography over the Grand Banks of Newfoundland, *Ocean Modelling.* 40, 199-210.
- Hart, D.J., deYoung, B., Foley, J., 1999. Observations of currents, temperature and salinity in Placentia Bay, Newfoundland. *Physics and Physical Oceanography Data Report 1998–9*, Memorial University of Newfoundland, St. John's: Newfoundland.
- Hogan, 2008. Assessment of the SmartBay Technology Demonstration Project: An Initiative of the Ocean Action Plan. ACOA-APECA
- Hubbard, M.E, 1999. Multidimensional slope limiters for MUSCL-type [mite volume schemes on unstructured grid. *J.comput.Phys.* 155,54-74.
- Jiang, L., and M. Xia (2016), Dynamics of the Chesapeake Bay outflow plume: Realistic plume simulation and its seasonal and interannual variability, *J. Geophys. Res. Oceans*, 121, 1424-1445, doi:10.1002/2015JC011191.

- Kobayashi, M.H., IM.C.Pereira and J.C.F.Pereira, 1999. A conservative finite volume second order accurate projection method on hybrid unstructured grids. *J.Comput.Phys.*, 150,40-75.
- Kolmogorov, A. N., 1941: Dissipation of energy in locally isotropic turbulence. *Dokl. Akad. Nauk SSSR*, 32, 19–21 (in Russian).
- Kraus, E. B. 1972. *Atmosphere-Ocean Interaction*. Clarendon Press, 275pp.
- Lawson, G.L., and G.A.Rose, 2000. Small-scale spatial and temporal patterns in spawning of Atlantic cod (*Gadus morhua*) in coastal Newfoundland waters. *Can.J.Fish.Aquat.Sci.*, 57, 1011-1024.
- LEVITUS, S. 1982. *Climatology atlas of the world ocean*. NOAA Professional Paper 13. U.S. Department of Commerce. Washington, DC.
- Ma, Z., 2010. *Simulation of temperature and currents in Placentia Bay*. Thesis (Master's degree) Memorial University of Newfoundland
- Ma, Z., Han, G., deYoung, B., 2012. Modelling temperature, currents and stratification in Placentia Bay. *J. Atmos. Ocean.* 50: 244-260.
- Ma, Z., Han, G., deYoung, B., 2015. Oceanic responses to hurricane Igor over the Grand Banks: a modelling study. *J. Geophys. Res. Oceans.* 120:doi:10.1002/2014JC010322.
- Ma, Z., 2015. *Simulation of Wind-Forced Responses over the Newfoundland Shelf*. Thesis (Ph. D.) Memorial University of Newfoundland
- Madala, R. V., and S. A. Piacsek. 1977. A semi-implicit numerical model for baroclinic oceans, *J. Comput. Phys.*, 23, 167-178.
- Mellor, G. L. and T. Yamada. 1982. Development of a turbulence closure model for geophysical fluid problem. *Rev. Geophys. Space. Phys.*, 20, 851-875.
- Mellor, G.L., T. Ezer and L.Y. Oey. 1993. The pressure gradient conundrum of sigma coordinate ocean models, *J. Atmos. Ocean. Tech.*, 11: 1126–1134.
- Mesinger, F., Dimego, G., Kalnay, E., Shafran, P., Ebisuzaki, W., Jovic, D., Wollen, J., Mitchell, K., Rogers, E., Fan, M., Ek, Y., Grumbine, R., Higgins, W., Li, H., Lin, Y., Manikin, G., Parrish, D., Shi, W., 2006. North American Regional Reanalysis. *Bull. Amer. Meteor. Soc.* 87, 343-360.
- Miles, J. W., 1961: On the stability of heterogeneous shear flows. *J. Fluid Mech.*, 10, 496–508.
- Petrie, B., and C. Anderson, 1983. Circulation on the Newfoundland continental shelf, *Atmos. Ocean*, 21, 207-226.

Rose, G.A., deYoung, B., Kulka, D.W., Goddard, S.V., and Fletcher, G.L., 1999. Distribution shifts and overfishing the northern cod (*Gadus morhua*): a view from the ocean. *Can. J. Fish. Aquat. Sci.*, 57, 644-664.

Schillinger, D.J., Simmons, P., deYoung, B., 2000. Analysis of the mean circulation in Placentia Bay: spring and summer 1999. Physics and physical oceanography data report 2000-1, Memorial University of Newfoundland: St. Johns, Newfoundland.

Sheng, J., and K. Thompson (1996), Surface circulation on the Newfoundland Shelf and Grand Banks: The roles of local density gradients and remote forcing, *Atmos. Ocean*, 43, 257–284.

Silva, I.P.D., A. Brandt, L. J. Montenegro and H. J. S. Fernando. 1999. Gradient Richardson number measurements in a stratified shear layer. *Dynam. Atmos. Oceans*. 20(1), 47-64.

Simpson, J. J. and T. D. Dickey, 1981a: The relationship between downward irradiance and upper ocean structure. *J. Phys. Oceanogr.*, 11, 309-323.

Simpson, J. J. and T. D. Dickey, 1981b: Alternative parameterizations of downward irradiance and their dynamical significance. *J. Phys. Oceanogr.*, 11, 876-882.

Smagorinsky, J. 1963. General circulation experiments with the primitive equations, I. The basic experiment. *Monthly Weather Review*, 91:99-164.

Snelgrove, P.V.R., Bradbury, I.R., deYoung, B. and Fraser, S., 2008. Temporal variation in fish egg and larval production by pelagic and bottom spawners in a large Newfoundland coastal embayment, *Journal of fisheries and aquatic sciences*, vol 65, 159-175.

Urrego-Blanco, J. and J. Sheng. 2012. Interannual variability of the circulation over the Eastern Canadian Shelf. *Atmosphere-Ocean*. 50, 277-300.